Improved aerosol correction for OMI tropospheric NO_2 retrieval over East Asia: constraint from CALIOP aerosol vertical profile

Mengyao Liu[1,2], Jintai Lin[1], K. Folkert Boersma[2,3], Gaia Pinardi[4], Yang Wang[5], Julien Chimot[6], Thomas Wagner[5], Pinghua Xie[7,8,9], Henk Eskes[2], Michel Van Roozendael[4], François Hendrick[4], Pucai Wang[10], Ting Wang[10], Yingying Yan[1], Lulu Chen[1], Ruijing Ni[1]

1, Laboratory for Climate and Ocean-Atmosphere Studies, Department of Atmospheric and Oceanic Sciences, School of Physics, Peking University, Beijing, China

2, Royal Netherlands Meteorological Institute, De Bilt, the Netherlands

3, Meteorology and Air Quality department, Wageningen University, Wageningen, the Netherlands

4, Royal Belgian Institute for Space Aeronomy (BIRA-IASB), Brussels, Belgium

5, Max Planck Institute for Chemistry, Mainz, Germany

6, Department of Geoscience and Remote Sensing (GRS), Civil Engineering and Geosciences, TU Delft, the Netherlands

7, Anhui Institute of Optics and Fine Mechanics, Key laboratory of Environmental Optics and Technology, Chinese Academy of Sciences, Hefei, China

8, CAS Center for Excellence in Urban Atmospheric Environment, Institute of Urban Environment, Chinese Academy of Sciences, Xiamen, China

9, School of Environmental Science and Optoelectronic Technology, University of Science and Technology of China, Hefei, China

10, IAP/CAS, Institute of Atmospheric Physics, Chinese Academy of Sciences, Beijing, China

Correspondence to: Jintai Lin (linjt@pku.edu.cn); K. Folkert Boersma (folkert.boersma@knmi.nl)

Abstract

Satellite retrieval of vertical column densities (VCDs) of tropospheric nitrogen dioxide (NO_2) is critical for NO_x pollution and impact evaluation. For regions with high aerosol loadings, the retrieval accuracy is greatly affected by whether aerosol optical effects are treated implicitly (as additional "effective" clouds) or explicitly, among other factors. Our previous POMINO algorithm explicitly accounts for aerosol effects to improve the retrieval especially in polluted situations over China, by using aerosol information from GEOS-Chem simulations with further monthly constraints by MODIS/Aqua aerosol optical depth (AOD) data. Here we present a major algorithm update, POMINO v1.1, by constructing a monthly climatological data set of aerosol extinction profiles, based on Level-2 CALIOP/CALIPSO data over 2007–2015, to better constrain the modeled aerosol vertical profiles.

We find that GEOS-Chem captures the month-to-month variation of CALIOP aerosol layer height but with a systematic underestimate by about 300–600 m (season and location dependent), due to a too strong negative vertical gradient of extinction above 1 km. Correcting the model aerosol extinction profiles results in small changes in retrieved cloud fraction, increases in cloud top pressure (within 2–6% in most cases), and increases in tropospheric NO_2 VCD by 4–16% over China on a monthly basis in 2012. The improved NO_2 VCDs (in POMINO v1.1) are more consistent with independent ground-based MAX-DOAS observations (R^2 = 0.80, NMB = -3.4%, for 162 pixels in 49 days) than POMINO (R^2 = 0.80, NMB = -9.6%), DOMINO v2 (R^2 =

0.68, NMB = -2.1%) and QA4ECV (R^2 = 0.75, NMB = -22.0%) are. Especially on haze days, R^2 reaches 0.76 for POMINO v1.1, much higher than that for POMINO (0.68), DOMINO v2 (0.38) and QA4ECV (0.34). Furthermore, the increase in cloud pressure likely reveals a more realistic vertical relationship between cloud and aerosol layers, with aerosols situated above the clouds in certain months instead of always below the clouds. The POMINO v1.1 algorithm is a core step towards our next public release of data product (POMINO v2), and it will also be applied to the recently launched S5P-TropOMI sensor.

1. Introduction

Air pollution is a major environmental problem in China. In particular, China has become the world's largest emitting country of nitrogen oxides (NO_X=NO+NO_2) due to its rapid economic growth, heavy industries, coal-dominated energy sources, and relatively weak emission control (Cui et al., 2016; Lin et al., 2014a; Stavrakou et al., 2016; Zhang et al., 2009). Tropospheric vertical column densities (VCDs) of nitrogen dioxide (NO_2) retrieved from the Ozone Monitoring Instrument (OMI) onboard the Earth Observing System (EOS) Aura satellite have been widely used to monitor and analyze NO_X pollution over China because of its high spatiotemporal coverage (e.g. (Lin et al., 2010; Miyazaki and Eskes, 2013; Verstraeten et al., 2015; Zhao and Wang, 2009). However, NO_2 retrieved from OMI and other space-borne instruments are subject to errors in the conversion process from radiance to VCD, particularly with respect to the calculation of tropospheric air mass factor (AMF) that is used to convert tropospheric slant column density to VCD (e.g. Boersma et al., 2011; Bucsela et al., 2013; Lin et al., 2015; Lorente et al., 2017).

Most current-generation NO_2 algorithms do not explicitly account for the effects of aerosols on NO_2 AMFs and on prerequisite cloud parameter retrievals. These retrievals often adopt an implicit approach wherein cloud algorithms retrieve "effective cloud"

parameters that include the optical effects of aerosols. This implicit method is based on aerosols exerting an effect on the top-of-atmosphere radiance level, whereas the assumed cloud model does not account for the presence of aerosols in the atmosphere (Stammes et al., 2008; Veefkind et al., 2016; Wang et al., 2008b; Wang and Stammes, 2014). In the absence of clouds, an aerosol optical thickness of 1 is then interpreted as an effective cloud fraction of ± 0.10, and the value also depends on the aerosol properties (scattering or absorbing), true surface albedo and geometry angles (Chimot et al., 2016) with an effective cloud pressure closely related to the aerosol layer, at least for aerosols of predominantly scattering nature (e.g. Boersma et al., 2004, 2011, Castellanos et al., 2014, 2015). However, in polluted situations with high aerosol loadings and more absorbing aerosol types, which often occur over China and many other developing regions, the implicit method can result in considerable biases (Castellanos et al., 2014, 2015; Chimot et al., 2016; Kanaya et al., 2014; Lin et al., 2014b).

Lin et al. (2014b, 2015) established the POMINO NO_2 algorithm, which builds on the DOMINO v2 algorithm (for OMI NO_2 slant columns and stratospheric correction), but improves upon it through a more sophisticated AMF calculation over China. In POMINO, the effects of aerosols on cloud retrievals and NO_2 AMFs are explicitly accounted for. In particular, daily information on aerosol optical properties such as aerosol optical depth (AOD), single scattering albedo (SSA), phase function and vertical extinction profiles are taken from nested Asian GEOS-Chem v9-02 simulations. The modeled AOD at 550 nm is further constrained by MODIS/Aqua monthly AOD, with the correction applied to other wavelengths based on modeled aerosol refractive indices (Lin et al., 2014b). However, the POMINO algorithm does not include an observation-based constraint on the vertical profile of aerosols, whose altitude relative to NO_2 has strong and complex influences on NO_2 retrieval (Castellanos et al., 2015; Leitão et al., 2010; Lin et al., 2014b). This study improves upon the POMINO algorithm

by incorporating CALIOP monthly climatology of aerosol vertical extinction profiles to correct for model biases.

The CALIOP lidar, carried on the sun-synchronous CALIPSO satellite, has been acquiring global aerosol extinction profiles since June 2006 (Winker et al., 2010). CALIPSO and Aura are both parts of the National Aeronautics and Space Administration (NASA) A-train constellation of satellites. The overpass time of CALIOP/CALIPSO is only 15 minutes later than OMI/Aura. In spite of issues with the detection limit, radar ratio selection and cloud contamination that cause some biases in CALIOP aerosol extinction vertical profiles (Amiridis et al., 2015; Koffi et al., 2012; Winker et al., 2013), comparisons of aerosol extinction profiles between ground-based lidar and CALIOP show good agreements (Kacenelenbogen et al., 2014; Kim et al., 2009; Misra et al., 2012). However, CALIOP is a nadir-viewing instrument that measures the atmosphere along the satellite ground-track with a narrow field-of-view. This means that the daily geographical coverage of CALIOP is much smaller than that of OMI. Thus previous studies often used monthly/seasonal regional mean CALIOP data to study aerosol vertical distributions or to evaluate model simulations (Chazette et al., 2010; Johnson et al., 2012; Koffi et al., 2012; Ma and Yu, 2014; Sareen et al., 2010).

There exist a few CALIOP Level-3 gridded datasets, such as LIVAS (Amiridis et al. 2015) and NASA official Level-3 monthly dataset (Winker et al., 2013). However, LIVAS is an annual average day-night combined product, not suitable to be applied to OMI NO_2 retrievals (around early afternoon, and in need of a higher temporal resolution than annual). The horizontal resolution (2° long. × 5° lat.) of NASA official product is much coarser than OMI footprints and the GEOS-Chem model resolution.

Here we construct a custom monthly climatology of aerosol vertical extinction profiles based on 9-years (2007–2015) worth of CALIOP Version 3 Level-2 532 nm data. On a

climatological basis, we use the CALIOP monthly data to adjust GEOS-Chem profiles in each grid cell for each day of the same month in any year. We then use the corrected GEOS-Chem vertical extinction profiles in the retrievals of cloud parameters and NO_2. Finally, we evaluate our updated POMINO retrieval (hereafter referred to as POMINO v1.1), our previous POMINO product, DOMINO v2 and the newly released Quality Assurance for Essential Climate Variables product (QA4ECV, see Appendix A), using ground-based MAX-DOAS NO_2 column measurements at three urban/suburban sites in East China for the year of 2012 and several months in 2008/2009.

Section 2 describes the construction of CALIOP aerosol extinction vertical profile monthly climatology, the POMINO v1.1 retrieval approach, and the MAX-DOAS data. It also presents the criteria for comparing different NO_2 retrieval products and for selecting coincident OMI and MAX-DOAS data. Section 3 compares our CALIOP climatology with NASA's official Level-3 CALIOP dataset and GEOS-Chem simulation results. Sections 4 and 5 compare POMINO v1.1 to POMINO to analyze the influence of improved aerosol vertical profiles on retrievals of cloud parameters and NO_2 VCDs, respectively. Section 6 evaluates POMINO, POMINO v1.1, DOMNO v2 and QA4ECV NO_2 VCD products using the MAX-DOAS data. Section 7 concludes our study.

2. Data and methods

2.1 CALIOP monthly mean extinction profile climatology

CALIOP is a dual-wavelength polarization lidar measuring attenuated backscatter radiation at 532 and 1064 nm since June 2006. The vertical resolution of aerosol extinction profiles is 30 m below 8.2 km and 60 m up to 20.2 km (Winker et al., 2013), with a total of 399 sampled altitudes. The horizontal resolution of CALIOP scenes is

335 m along the orbital track and is given over a 5 km horizontal resolution in Level-2 data.

As detailed in Appendix B, we use the daily all-sky Version 3 CALIOP Level-2 aerosol profile product at 532 nm from 2007 to 2015 to construct a monthly Level-3 climatological dataset of aerosol extinction profiles over China and nearby regions. This dataset is constructed on the GEOS-Chem model grid (0.667° long. x 0.5° lat.) and vertical resolution (47 layers, with 36 layers or so in the troposphere). The ratio of climatological monthly CALIOP to monthly GEOS-Chem profiles represents the scaling profile to adjust the daily GEOS-Chem profiles in the same month (see Sect. 2.2)

2.2 POMINO v1.1 retrieval approach

The NO_2 retrieval consists of three steps. First, the total NO_2 slant columns density (SCD) is retrieved using the Differential Optical Absorption Spectroscopy (DOAS) technique (for the 405-465 nm spectral window in the case of OMI). The uncertainty of the SCD is determined by the appropriateness of the fitting technique, the instrument noise, the choice of fitting window, and the orthogonality of the absorbers' cross sections (Bucsela et al., 2006; van Geffen et al., 2015; Lerot et al., 2010; Richter et al., 2011; Zara et al., 2018). The NO_2 SCD in DOMINO v2 has a bias at about 0.5~1.3 × 10^{15} molec. cm^{-2} (Belmonte Rivas et al., 2014; Dirksen et al., 2011; van Geffen et al., 2015; Marchenko et al., 2015; Zara et al., 2018), which can be reduced by improving wavelength calibration and including O_2-O_2 and liquid water absorption in the fitting model (van Geffen et al., 2015; Zara et al., 2018). The tropospheric SCD is then obtained by subtracting the stratospheric SCD from the total SCD. The bias in the total SCD is mostly absorbed by this stratospheric separation step, which may not propagate into the tropospheric SCD (van Geffen et al., 2015). The last step converts the tropospheric SCD to VCD by using the tropospheric AMF (VCD = SCD / AMF). The

tropospheric AMF is calculated at 438 nm by using look-up tables (in most retrieval algorithms) or online radiative transfer modeling (in POMINO) driven by ancillary parameters, which act as the dominant source of errors in retrieved NO_2 VCD data over polluted areas (Boersma et al., 2007; Lin et al., 2014b, 2015; Lorente et al., 2017).

Our POMINO algorithm focuses on the tropospheric AMF calculation over China and nearby regions, taking the tropospheric SCD (Dirksen et al., 2011) from DOMINO v2 (Boersma et al., 2011). POMINO improves upon the DOMINO v2 algorithm in the treatment of aerosols, surface reflectance, online radiative transfer calculations, spatial resolution of NO_2, temperature and pressure vertical profiles, and consistency between cloud and NO_2 retrievals (Lin et al., 2014b, 2015). In brief, we use the parallelized LIDORT-driven AMFv6 package to derive both cloud parameters and tropospheric NO_2 AMFs for individual OMI pixels online. NO_2 vertical profiles, aerosol optical properties and aerosol vertical profiles are taken from the nested GEOS-Chem model over Asia (0.667° long.$\times 0.5^\circ$ lat. before May 2013 and 0.3125° long.$\times 0.25^\circ$ lat. afterwards), and pressure and temperature profiles are taken from the GEOS-5 and GEOS-FP assimilated meteorological fields that drive GEOS-Chem simulations. Model aerosols are further adjusted by satellite data (see below). We adjust the pressure profiles based on the difference in elevation between the pixel center and the matching model grid cell (Zhou et al., 2010). We also account for the effects of surface bidirectional reflectance distribution function (BRDF) (Lin et al., 2014b; Zhou et al., 2010) by taking three kernel parameters (isotropic, volumetric and geometric) from the MODIS MCD43C2 data set at 440 nm (Lucht et al., 2000).

As a prerequisite to the POMINO NO_2 retrieval, clouds are retrieved through the O_2-O_2 algorithm (Acarreta et al., 2004; Stammes et al., 2008) with O_2-O_2 SCDs from OMCLDO2, and with pressure, temperature, surface reflectance, aerosols and other ancillary information consistent with the NO_2 retrieval. Note that the treatment of cloud

scattering (as "effective" Lambertian reflector, as in other NO_2 algorithms) is different from the treatment of aerosol scattering/absorption (vertically resolved based on the Mie scheme).

POMINO uses the temporally and spatially varying aerosol information, including AOD, single scattering albedo (SSA), phase function and vertical profiles from GEOS-Chem simulations. POMINO v1.1 (this work) further uses CALIOP data to constrain the shape of aerosol vertical extinction profile. We run the model at a resolution of 0.3125° long.×0.25° lat. before May 2013 and 0.667° long.×0.5° lat. afterwards, as determined by the resolution of the driving meteorological fields. We then regrid the finer resolution model results to 0.667° long.×0.5° lat., to be consistent with the CALIOP data grid. We then sample the model data at times and locations with valid CALIOP data at 532 nm to establish the model monthly climatology.

For any month in a grid cell, we divide the CALIOP monthly climatology of aerosol extinction profile shape by model climatological profile shape to obtain a unitless scaling profile (Eq. 1), and apply this scaling profile to all days of that month in all years (Eq. 2). Such a climatological adjustment is based on the assumption that systematic model limitations are month-dependent and persist over the years and days (e.g., a too strong vertical gradient, see Sect. 3.3). Although this monthly adjustment means discontinuity on the day-to-day basis (e.g., from the last day of a month to the first day of the next month), such discontinuity does not significantly affect the NO_2 retrieval, based on our sensitivity test.

In Eqs. 1 and 2, E^C represents the CALIOP climatological aerosol extinction coefficient, E^G the GEOS-Chem extinction, E^{Gr} the post-scaling model extinction, and R the scaling profile. The subscript *i* denotes a grid cell, *k* a vertical layer, *d* a day, *m* a month, and *y* a year. Note that in Eq. 1, the extinction coefficient at each layer is normalized relative to the maximum value of that profile. This procedure ensures that

the scaling is based on the relative shape of the extinction profile and is thus independent of the accuracies of CALIOP and GEOS-Chem AOD. We keep the absolute AOD value of GEOS-Chem unchanged in this step.

$$R_{i,k,m} = \frac{E^{C}_{i,k,m}/\max\left(E^{C}_{i,k,m}\right)}{E^{G}_{i,k,m}/max\left(E^{G}_{i,k,m}\right)} \quad (1)$$

$$E^{Gr}_{i,k,d,m,y} = E^{G}_{i,k,d,m,y} \times R_{i,k,m} \quad (2)$$

In POMINO, the GEOS-Chem AOD are further constrained by a MODIS/Aqua Collection 5.1 monthly AOD dataset compiled on the model grid (Lin et al., 2014b, 2015). POMINO v1.1 uses the Collection 5.1 AOD data before May 2013 and Collection 6 data afterwards. For adjustment, model AOD are projected to a 0.667° long.×0.5° lat. grid and then sampled at times and locations with valid MODIS data (Lin et al., 2015). As shown in Eq. 3, τ^{M} denotes MODIS AOD, τ^{G} GEOS-Chem AOD, and τ^{Mr} post-adjustment model AOD. The subscript *i* denotes a grid cell, *d* a day, *m* a month, and *y* a year. This AOD adjustment ensures that in any month, monthly mean GEOS-Chem AOD is the same as MODIS AOD while the modeled day-to-day variability is kept.

$$\tau^{Gr}_{i,d,m,y} = \frac{\tau^{M}_{i,m,y}}{\tau^{G}_{i,m,y}} \times \tau^{G}_{i,d,m,y} \quad (3)$$

Equations 4–5 show the complex effects of aerosols in calculating the AMF for any pixel. The AMF is the linear sum of tropospheric layer contributions to the slant column weighted by the vertical sub columns (Eq. 4). The box AMF, amf_k, describes the sensitivity of NO_2 SCD to layer k, and $x_{a,k}$ represent the subcolumn of layer k from a priori NO_2 profile. The l represent the first integrated layer, which is the layer above the ground for clear sky, or the layer above cloud top for cloudy sky. The t represent the tropopause layer. POMINO assumes the independent pixel approximation (IPA)

(Martin et al., 2002; Boersma et al., 2002). This means that the calculated AMF for any pixel consists of a fully cloudy-sky portion (AMF_{clr}) and a fully clear-sky portion (AMF_{cld}), with weights based on the cloud radiance fraction ($\mathrm{CRF} = (1 - \mathrm{CF}) \cdot \mathrm{A_{clr}} + \mathrm{CF} \cdot \mathrm{A_{cld}}$, where $\mathrm{A_{clr}}$, $\mathrm{A_{cld}}$ are radiance from the clear-sky part and fully cloudy part of the pixel, respectively.) (Eq. 5). AMF_{cld} is affected by above-cloud aerosols, and AMF_{clr} is affected by aerosols in the entire column. Also, aerosols affect the retrieval of CRF. Thus, the improvement of aerosol vertical profile in POMINO v1.1 affects all the three quantities in Eq. 5 and thus leads to complex impacts on retrieved NO_2 VCD.

$$\mathrm{AMF} = \frac{\sum_l^t amf_k x_{a,k}}{\sum_l^t x_{a,k}} \quad (4)$$

$$\mathrm{AMF} = \mathrm{AMF}_{cld} \cdot \mathrm{CRF} + \mathrm{AMF}_{clr} \cdot (1 - \mathrm{CRF}) \quad (5)$$

2.3 OMI pixel selection to evaluate POMINO v1.1, POMINO, DOMINO v2 and QA4ECV

We exclude OMI pixels affected by row anomaly (Schenkeveld et al., 2017) or with high albedo caused by icy/snowy ground. To screen out cloudy scenes, we choose pixels with CRF below 50% (effective cloud fraction is typically below 20%) in POMINO.

The selection of CRF threshold influences the validity of pixels. The "effective" CRF in DOMINO implicitly includes the influence of aerosols. In POMINO, the aerosol contribution is separated from that of the clouds, resulting in a lower CRF than for DOMINO. The CRF differs insignificantly between POMINO and POMINO v1.1, because the same AOD and other non-aerosol ancillary parameters are used in the retrieval process. Using the CRF from POMINO instead of DOMINO or QA4ECV for cloud screening means that the number of "valid" pixels in DOMINO increases by about 25%, particularly because much more pixels with high pollutant (aerosol and NO_2)

loadings are now included. This potentially reduces the sampling bias (Lin et al., 2014b, 2015), and the ensemble of pixels now includes scenes with high "aerosol radiative fractions". Further research is needed to fully understand how much these high-aerosol scenes may be subject to the same screening issues as the cloudy scenes. Nevertheless, the limited evidence here and in Lin et al. (2014b, 2015) suggests that including these high-aerosol scenes does not affect the accuracy of NO_2 retrieval.

2.4 MAX-DOAS data

We use MAX-DOAS measurements at three suburban or urban sites in East China, including one urban site at the Institute of Atmospheric Physics (IAP) in Beijing (116.38° E, 39.38° N), one suburban site in Xianghe County (116.96° E, 39.75° N) to the south of Beijing, and one urban site in the Wuxi City (120.31° E, 31.57° N) in the Yangzi River delta (YRD). Figure 1 shows the locations of these sites overlaid with POMINO v1.1 NO_2 VCDs in August 2012. Table 1 summarizes the information of MAX-DOAS measurements.

The instruments in IAP and in Xianghe were designed at BIRA-IASB (Clémer et al., 2010). Such an instrument is a dual-channel system composed of two thermally regulated grating spectrometers, covering the ultraviolet (300–390 nm) and visible (400–720 nm) wavelengths. It measures scattered sunlight every 15 minutes at nine elevation angles: 2°, 4°, 6°, 8°, 10°, 12°, 15°, 30°, and 90°. The telescope of the instrument is pointed to the north. The data are analyzed following Hendrick et al. (2014). The Xianghe suburban site is influenced by pollution from the surrounding major cities like Beijing and Tianjin. At Xianghe, MAX-DOAS data are data are continuously available since early 2011, and data in 2012 are used here for comparison with OMI products. At IAP, MAX-DOAS data are available in 2008 and 2009 (Table 1), thus for comparison purposes we process OMI products to match the MAX-DOAS times.

Located on the roof of an 11-story building, the instrument at Wuxi was developed by Anhui Institute of Optics and Fine Mechanics (AIOFM) (Wang et al., 2015, 2017a). Its telescope is pointed to the north and records at five elevation angles (5°, 10°, 20°, 30° and 90°). Wuxi is a typical urban site affected by heavy NO_x and aerosol pollution. The measurements used here are analyzed in Wang et al. (2017a). Data are available in 2012 for comparison with OMI products.

When comparing the four OMI products against MAX-DOAS observations, temporal and spatial inconsistency in sampling is inevitable. The spatial inconsistency, together with the substantial horizontal inhomogeneity in NO_2, might be more important than the influence of temporal inconsistency (Wang et al., 2017b). The influence of the horizontal inhomogeneity was suggested to be about 10–30% for MAX-DOAS measurements in Beijing (Lin et al., 2014b; Ma et al., 2013) and 10–15% for less polluted locations like Tai'an, Mangshan and Rudong (Irie et al., 2012). Following previous studies (Lin et al., 2014b; Wang et al., 2015, 2017b), we average MAX-DOAS data within 2 h of the OMI overpass time, and we select OMI pixels within 25 km of a MAX-DOAS site whose viewing zenith angle is below 30°. To exclude local pollution events near the MAX-DOAS site (such as the abrupt increase of NO_2 caused by the pass of consequent vehicles during a very short period), the standard deviation of MAX-DOAS data within 2 h should not exceed 20% of their mean value (Lin et al., 2014b). We elect not to spatially average the OMI pixels because they can, to some degree, reflect the spatial variability in NO_2 and aerosols.

We further exclude MAX-DOAS data in cloudy conditions, as clouds can cause large uncertainties in MAX-DOAS and OMI data. To find the actual cloudy days, we use MODIS/Aqua cloud fraction data, MODIS/Aqua Level-3 corrected reflectance (true color) data at the $1° \times 1°$ resolution, and current weather data observed from the nearest ground meteorological station (indicated by the black triangles in Fig. 1b).

Since there is only one meteorological station available near the Beijing area, it is used for both IAP and Xianghe MAX-DOAS sites. We first use MODIS/Aqua corrected reflectance (true color) to distinguish clouds from haze. For cloudy days determined by the reflectance checking, we examine both the MODIS/Aqua cloud fraction data and the meteorological station cloud records, considering that MODIS/Aqua cloud fraction data may be missing or have a too coarse horizontal resolution to accurately interpret the cloud conditions at the MAX-DOAS site. We exclude MAX-DOAS NO_2 data if the MODIS/Aqua cloud fraction is larger than 60% and the meteorological station reports a "BROKEN" (cloud fraction ranges from 5/8 to 7/8) or "OVERCAST" (full cloud cover) sky. For the three MAX-DOAS sites together, this leads to 49 days with valid data out of 64 days with pre-screening data.

We note here that using cloud fraction data from MODIS/Aqua or MAX-DOAS (for Xianghe only, see Gielen et al., 2014) alone to screen cloudy scenes may not be appropriate on heavy-haze days. For example, on 8th January, 2012, MODIS/Aqua cloud fraction is about 70–80% over the North China Plain and MAX-DOAS at Xianghe suggests the presence of "thick clouds". However, both the meteorological station and MODIS/Aqua corrected reflectance (true color) product suggest that the North China Plain was covered by a thick layer of haze. Consequently, this day was excluded from the analysis.

3. Monthly climatology of aerosol extinction profiles from CALIOP and GEOS-Chem

3.1 CALIOP monthly climatology

The aerosol layer height (ALH) is a good indicator to what extent aerosols are mixed vertically (Castellanos et al., 2015). As defined in Eq. A1 in Appendix B, the ALH is the average height of aerosols weighted by vertically resolved aerosol extinction. Figure

2a shows the spatial distribution of our CALIOP ALH climatology in each season. At most places, the ALH reaches a maximum in spring or summer and a minimum in fall or winter. The lowest ALH in fall and winter can be attributed to heavy near-surface pollution and weak vertical transport. The high values in summer are related to strong convective activities. Over the north, the high values in spring are partly associated with Asian dust events, due to high surface winds and dry soil in this season (Huang et al., 2010; Proestakis et al., 2017; Wang et al., 2010), which also affects the oceanic regions via atmospheric transport. The springtime high ALH over the south may be related to the transport of carbonaceous aerosols from Southeast Asian biomass burning (Jethva et al., 2016). Averaged over the domain, the seasonal mean ALHs are 1.48 km, 1.43 km, 1.27km, 1.18 km in spring, summer, fall and winter.

Figure 3a,b further shows the climatological monthly variations of ALH averaged over Northern East China (the anthropogenic source region shown in orange in Fig. 1a) and Northwest China (the dust source region shown in yellow in Fig. 1a). The two regions exhibit distinctive temporal variations. Over Northern East China, the ALH reaches a maximum in April (~1.53 km) and a minimum in December (~1.14 km). Over Northwest China, the ALH peaks in August (~1.59km) because of strongest convection (Zhu et al., 2013), although the springtime ALH is also high.

Figure 4a shows the climatological seasonal regional average vertical profiles of aerosol extinction over Northern East China. Here, the aerosol extinction increases from the ground level to a peak at about 300–600 m (season dependent), above which it decreases gradually. The height of peak extinction is lowest in winter, consistent with a stagnant atmosphere, thin mixing layer, and increased emissions (from residential and industrial sectors). The large error bars (horizontal lines in different layers, standing for 1 standard deviation) indicate strong spatiotemporal variability of aerosol extinction.

Over Northwest China (Fig. 5a), the column total aerosol extinction is much smaller than that over Northern East China (Fig. 4a), due to lower anthropogenic sources and dominant natural dust emissions. Vertically, the decline of extinction from the peak-extinction height to 2 km is also much more gradual than the decline over Northern East China, indicating stronger lifting of surface emitted aerosols. In winter, the column total aerosol extinction is close to the high value in dusty spring, whereas the vertical gradient of extinction is strongest among the seasons. This reflects the high anthropogenic emissions in parts of Northwest China, which have been rapidly increasing in the 2000s due to relatively weak emission control supplemented by growing activities of relocation of polluted industries from the eastern coastal regions (Cui et al., 2016; Zhao et al., 2015).

Overall, the spatial and seasonal variations of CALIOP aerosol vertical profiles are consistent with changes in meteorological conditions, anthropogenic sources, and natural emissions. The data will be used to evaluate and adjust GEOS-Chem simulation results in Sect. 3.2. A comparison of our CALIOP dataset with NASA's official Level-3 data is presented in Appendix C.

3.2 Evaluation of GEOS-Chem aerosol extinction profiles

Figure 2b shows the spatial distribution of seasonal ALHs simulated by GEOS-Chem. The model captures the spatial and seasonal variations of CALIOP ALH (Fig. 2a) to some degree, with an underestimate by about 0.3 km on average. The spatial correlation between CALIOP (Fig. 2a) and GEOS-Chem (Fig. 2b) ALH is 0.37 in spring, 0.57 in summer, 0.40 in fall, and 0.44 in winter. The spatiotemporal consistency and underestimate is also clear from the regional mean monthly ALH data in Fig. 3 – the temporal correlation between GEOS-Chem and CALIOP ALH is 0.90 in Northern East China and 0.97 in Northwest China.

Figures 4a and 5a show the GEOS-Chem simulated 2007–2015 monthly climatological vertical profiles of aerosol extinction coefficient over Northern East China and Northwest China, respectively. Over Northern East China (Fig. 4a), the model (red line) captures the vertical distribution of CALIOP extinction (black line) below the height of 1 km, despite a slight underestimate in the magnitude of extinction and an overestimate in the peak-extinction height. From 1 to 5 km above the ground, the model substantially overestimates the rate of decline in extinction coefficient with increasing altitude. Across the seasons, GEOS-Chem underestimates the magnitude of aerosol extinction by up to 37% (depending on the height). Over Northwest China (Fig. 5a), GEOS-Chem has an underestimate in all seasons, with the largest bias by about 80% in winter likely due to underestimated water-soluble aerosols and dust emissions (Li et al., 2016; Wang et al., 2008a).

Since the POMINO v1.1 algorithm uses MODIS AOD to adjust model AOD, it only uses the CALIOP aerosol extinction profile shape to adjust the modeled shape (Eqs. 1 and 2). Figures 4b and 4b show the vertical shapes of aerosol extinction, averaged across all profiles in each season over Northern East China and Northwest China, respectively. Over Northern East China (Fig. 4b), GEOS-Chem underestimates the CALIOP values above 1 km by 52–71%. This underestimate leads to a lower ALH, consistent with the finding by van Donkelaar et al. (2013) and Lin et al. (2014b). Over Northwest China (Fig. 5b), the model also underestimates the CALIOP values above 1 km by 50–62%. These results imply the importance of correcting the modeled aerosol vertical shape prior to cloud and NO_2 retrievals.

4. Effects of aerosol vertical profile improvement on cloud retrieval in 2012

Figure 6a, b shows the monthly average ALH and cloud top height (CTH, corresponding to cloud pressure, CP) over Northern East China and Northwest China in 2012. In order to discuss the CTH, only cloudy days are analyzed here, by excluding

429 days with zero cloud fraction (CF = 0, clear-sky cases) in POMINO. Although "clear
430 sky" is used sometimes in the literature to represent low cloud coverage (e.g., CF < 0.2
431 or CRF < 0.5, Boersma et al., 2011; Chimot et al., 2016), here it strictly means CF = 0
432 while "cloudy sky" means CF > 0. About 62.7% of days contain non-zero fractions of
433 clouds over Northern East China, and the number is 59.1% for Northwest China. The
434 CF changes from POMINO to POMINO v1.1 (i.e., after aerosol vertical profile
435 adjustment) are negligible (within $\pm$0.5%, not shown) due to the same values of AOD
436 and SSA used in both products. This is because overall CF is mostly driven by the
437 continuum reflectance at 475 nm (mainly determined by AOD and surface reflectance,
438 which remain unchanged), which is independent of aerosol profile but CTH is driven
439 by the O_2-O_2 SCD, which is itself impacted by ALH.

440 Figure 6a, b shows that over the two regions, the CTH varies notably from one month
441 to another, whereas the ALH is much more stable across the months. Over Northern
442 East China, the ALH increases by 0.52 km from POMINO (orange dashed line) to
443 POMINO v1.1 (orange solid line) due to the CALIOP-based monthly climatological
444 adjustment. The increase in ALH means a stronger "shielding" effect of aerosols on the
445 O_2-O_2 absorbing dimer, which, in turn, results in a reduced CTH by 0.69 km on average.
446 For POMINO over Northern East China (Fig. 6a), the retrieved clouds usually extend
447 above the aerosol layer, i.e., the CTH (grey dashed line) is much larger than the ALH
448 (orange dashed line). Using the CALIOP climatology in POMINO v1.1 results in the
449 ALH higher than the CTH in fall and winter. The more elevated ALH is consistent with
450 the finding of Jethva et al. (2016) that a significant amount of absorbing aerosols resides
451 above clouds over Northern East China based on 11-year (2004–2015) OMI near-UV
452 observations.

453 The CTH in Northwest China is much lower than in Northern East China (Fig. 6a versus
454 7b). This is because the dominant type of actual clouds is (optically thin) cirrus over

455 western China (Wang et al., 2014), which is interpreted by the O_2-O_2 cloud retrieval
456 algorithm as reduced CTH (with cloud base from the ground). The reduction in CTH
457 from POMINO to POMINO v1.1 over Northwest China is also smaller than the
458 reduction over Northern East China, albeit with a similar enhancement in ALH, due to
459 lower aerosol loadings (Fig. 6c versus 6d).

460 Figure 7g,h presents the relative change in CP from POMINO to POMINO v1.1 as a
461 function of AOD (binned at an interval of 0.1) and changes in ALH from POMINO to
462 POMINO v1.1 (ΔALH, binned every 0.2 km) across all pixels in 2012 over Northern
463 East China. Results are separated for low cloud fraction (CF < 0.05 in POMINO, Fig.
464 7g) and modest cloud fraction (0.2 < CF < 0.3, Fig. 7h). The median of the CP changes
465 for pixels within each AOD and ΔALH bin is shown. Figure 7e,f presents the
466 corresponding numbers of occurrence under the two cloud conditions.

467 Figure 7 shows that over Northern East China, the increase in ALH is typically within
468 0.6 km for the case of CF < 0.05 (Fig. 7e), and the corresponding increase in CP is
469 within 6% (Fig. 7g). In this case, the average CTH (2.95 km in POMINO versus 1.58
470 km in POMINO v1.1) becomes much lower than the average ALH (1.06 km in
471 POMINO versus 1.98 km in POMINO v1.1). For the case with CF between 0.2 and 0.3,
472 the increase in ALH is within 1.2 km for most scenes (Fig. 7f), which leads to a CP
473 change of 2% (Fig. 7h), much smaller than the CP change for CF < 0.05 (Fig. 7g). This
474 is partly because the larger the CF is, the smaller a change in CF is required to
475 compensate for the ΔALH in the O_2-O_2 cloud retrieval algorithm. Furthermore, with
476 0.2 < CF < 0.3, the mean value of CTH is much higher than ALH in both POMINO
477 (2.76 km for CTH versus 1.13km for ALH) and POMINO v1.1 (2.60km for CTH versus
478 2.09 km for ALH), thus a large portion of clouds are above aerosols so that the change
479 in CP is less sensitive to ΔALH. We find that the summertime data contribute the
480 highest portion (36.5%) to the occurrences for 0.2 < CF < 0.3.

For Northwest China (not shown), the dependence of CP changes to AOD and ΔALH is similar to that for Northern East China. In particular, the CP change is within 10% on average for the case of CF < 0.05 and 1.5% for the case of 0.2 < CF < 0.3.

5. Effects of aerosol vertical profile improvement on NO_2 retrieval in 2012

Figure 7a presents the percentage changes in clear-sky NO_2 VCD from POMINO to POMINO v1.1 as a function of binned AOD and ΔALH over Northern East China. Here, clear-sky pixels are chosen based on CF = 0 in POMINO. In any AOD bin, an increase in ΔALH leads to an enhancement in NO_2. And for any ΔALH, the change in VCD is greater (smaller) when AOD becomes larger (smaller), which indicates that the NO_2 retrieval is more sensitive to ALH in high aerosol loading cases. Clearly, the change in NO_2 is not a linear function of AOD and ΔALH.

For cloudy scenes (Fig. 7b,c, cloud data are based on POMINO), the change in NO_2 VCD is less sensitive to AOD and ΔALH. This is because the existence of clouds limits the optical effect of aerosols on tropospheric NO_2. Figure 6a presents the nitrogen layer height (NLH, defined as the average height of model simulated NO_2 weighted by its volume mixing ratio in each layer) in comparison to the ALH and CLH over Northern East China. The figure shows that the POMINO v1.1 CTH is higher than the NLH in all months and higher than the ALH in warm months, which means a "shielding" effect on both NO_2 and aerosols.

Over Northwest China (not shown), the changes in clear-sky NO_2 VCD are within 9% for most cases, which are much smaller than over Eastern China (within 18%). This is because the NLH is much higher than the CLH and ALH (Fig. 6b) in absence of surface anthropogenic emissions.

We convert the valid pixels into monthly mean Level-3 values datasets on a 0.25° long. × 0.25° lat. grid. Figure 8a,b compares the seasonal spatial variations of NO_2 VCD in POMINO v1.1 and POMINO in 2012. In both products, NO_2 peaks in winter due to the longest lifetime and highest anthropogenic emissions (Lin, 2012). NO_2 also reaches a maximum over Northern East China as a result of substantial anthropogenic sources. From POMINO to POMINO v1.1, the NO_2 VCD increases by 3.4% (-67.5–41.7%) in spring for the domain average (range), 3.0% (-59.5–34.4%) in summer, 4.6% (-15.3–39.6%) in fall and 5.3% (-68.4–49.3%) in winter. The NO_2 change is highly dependent on the location and season. The increase over Northern East China is largest in winter, wherein the positive value for ΔALH implies that elevated aerosol layers "shield" the NO_2 absorption.

6. Evaluating satellite products using MAX-DOAS data

We use MAX-DOAS data, after cloud screening (Sect. 2.4), to evaluate DOMNO v2, QA4ECV, POMINO and POMINO v1.1. The scatterplots in Fig. 9a-d compare the NO_2 VCDs from 162 OMI pixels on 49 days with their MAX-DOAS counterparts. Different colors differentiate the seasons. The high values of NO_2 VCD ($> 30 \times 10^{15}$ molec. cm^{-2}) occur mainly in fall (blue) and winter (black). POMINO v1.1 and POMINO capture the day-to-day variability of MAX-DOAS data, i.e., $R^2 = 0.804$ and 0.799, respectively. The normalized mean bias (NMB) of POMINO v1.1 relative to MAX-DOAS data (-3.4%) is smaller than the NMB of POMINO (-9.6%). Also, the reduced major axis (RMA) regression shows that the slope for POMINO v1.1 (0.95) is closer to unity than the slope for POMINO (0.78). When all OMI pixels in a day are averaged (Fig. 9e,f), the correlation across the total of 49 days further increase for both POMINO v1.1 ($R^2 = 0.89$) and POMINO ($R^2 = 0.86$), whereas POMINO v1.1 still has a lower NMB (-3.7%) and better slope (0.96) than POMINO (-10.4% and 0.82, respectively). These

529 results suggest that correcting aerosol vertical profiles, at least on a climatology basis,
530 already leads to a significant improved NO_2 retrieval from OMI.

531 Figure 9 shows that DOMINO v2 is correlated with MAX-DOAS ($R^2 = 0.68$ in Fig. 9c
532 and 0.75 in Fig. 9g) but not as strong as POMINO and POMINO v1.1 for all days. The
533 discrepancy between DOMINO v2 and MAX-DOAS is particularly large for very high
534 NO_2 values ($> 70 \times 10^{15}$ molec. cm^{-2}). The R^2 for QA4ECV (0.75 in Fig. 9d and 0.82
535 in Fig. 9h) is slightly better than DOMINO, but the NMB is higher (-22.0% and -22.7%)
536 and the slope drops to 0.66. These results are consistent with the finding of Lin et al.
537 (2014b, 2015) that explicitly including aerosol optical effects improves the NO_2
538 retrieval.

539 Table 2 further shows the comparison statistics for 27 haze days. The haze days are
540 determined when both the ground meteorological station data and MODIS/Aqua
541 corrected reflectance (true color) data indicate a haze day. The table also lists AOD,
542 SSA, CF and MAX-DOAS NO_2 VCD, as averaged over all haze days. A large amount
543 of absorbing aerosols occurs on these haze days (AOD = 1.13, SSA = 0.90). The
544 average MAX-DOAS NO_2 VCD reaches 51.92×10^{15} molec. cm^{-2}. Among the four
545 satellite products, POMINO v1.1 has the highest R^2 (0.76) and the lowest bias (4.4%)
546 with respect to MAX-DOAS, whereas DOMINO v2 and QA4ECV reproduce the
547 variability to a limited extent ($R^2 = 0.38$ and 0.34, respectively). This is consistent with
548 the previous finding that the accuracy of DOMINO v2 is reduced for polluted, aerosol-
549 loaded scenes (Boersma et al., 2011; Chimot et al., 2016; Kanaya et al., 2014; Lin et
550 al., 2014b).

551 Table 3 shows the comparison statistics for 36 cloud-free days (CF = 0 in POMINO,
552 and AOD = 0.60 on average). Here, POMINO v1.1, POMINO and DONIMO v2 do not
553 show large differences in R^2 (0.53–0.56) and NMB (20.8–29.4%) with respect to MAX-
554 DOAS. QA4ECV has a higher R^2 (0.63) and a lower NMB (-5.83%), presumably

555 reflecting the improvements in this (EU-) consortium approach, at least in mostly cloud-
556 free situations. However, the R^2 values for POMINO and POMINO v1.1 are much
557 smaller than the R^2 values in haze days, whereas the opposite changes are true for
558 DOMINO v2 and QA4ECV. Thus, for this limited set of data, the changes from
559 DOMINO v2 and QA4ECV to POMINO and POMINO v1.1 mainly reflect the
560 improved aerosol treatment in hazy scenes. Further research may use additional MAX-
561 DOAS datasets to evaluate the satellite products more systematically.

562 **7. Conclusions**

563 This paper improves upon our previous POMINO algorithm (Lin et al., 2015) to retrieve
564 the tropospheric NO_2 VCDs from OMI, by compiling a 9-year (2007–2015) CALIOP
565 monthly climatology of aerosol vertical extinction profiles to adjust GEOS-Chem
566 aerosol profiles used in the NO_2 retrieval process. The improved algorithm is referred
567 to as POMINO v1.1. Compared to monthly climatological CALIOP data over China,
568 GEOS-Chem simulations tend to underestimate the aerosol extinction above 1 km, as
569 characterized by an underestimate in ALH by 300–600 m (seasonal and location
570 dependent). Such a bias is corrected in POMINO v1.1 by dividing, for any month and
571 grid cell, the CALIOP monthly climatological profile by the model climatological
572 profile to obtain a scaling profile and then applying the scaling profile to model data in
573 all days of that month in all years.

574 The aerosol extinction profile correction leads to an insignificant change in CF from
575 POMINO to POMINO v1.1, since the AOD and surface reflectance are unchanged. In
576 contrast, the correction results in a notably increase in CP (i.e., a decrease in CTH), due
577 to lifting of aerosol layers. The CP changes are generally within 6% for scenes with low
578 cloud fraction (CF < 0.05 in POMINO), and within 2% for scenes with modest cloud
579 fraction (0.2 < CF < 0.3 in POMINO).

580 The NO_2 VCDs increase from POMINO to POMINO v1.1 in most cases due to lifting
581 of aerosol layers that enhances the "shielding" of NO_2 absorption. The NO_2 VCD
582 increases by 3.4% (-67.5–41.7%) in spring for the domain average (range), 3.0% (-
583 59.5–34.4%) in summer, 4.6% (-15.3–39.6%) in fall and 5.3% (-68.4–49.3%) in winter.
584 The NO_2 changes highly season and location dependent, and are most significant for
585 wintertime Northern East China.

586 Further comparisons with independent MAX-DOAS NO_2 VCD data for 162 OMI
587 pixels in 49 days show good performance of both POMINO v1.1 and POMINO in
588 capturing the day-to-day variation of NO_2 (R^2=0.80, n=162), compared to DOMINO
589 v2 (R^2=0.67) and the new QA4ECV product (R^2=0.75). The NMB is smaller in
590 POMINO v1.1 (-3.4%) than in POMINO (-9.6%), with a slightly better slope (0.804
591 versus 0.784). On hazy days with high aerosol loadings (AOD = 1.13 on average),
592 POMINO v1.1 has the highest R^2 (0.76) and the lowest bias (4.4%) whereas DOMINO
593 and QA4ECV have difficulty in reproducing the day-to-day variability in MAX-DOAS
594 NO_2 measurements (R^2 = 0.38 and 0.34, respectively). The four products show small
595 differences in R^2 on clear-sky days (CF = 0 in POMINO, AOD = 0.60 on average),
596 among which QA4ECV shows a highest R^2 (0.63) and lowest NMB (-5.83%),
597 presumably reflecting the improvements in less polluted place such as Europe and the
598 US. Thus the explicit aerosol treatment (in POMINO and POMINO v1.1) and the
599 aerosol vertical profile correction (in POMINO v1.1) improves the NO_2 retrieval
600 especially in hazy cases.

601 The POMINO v1.1 algorithm is a core step towards our next public release of data
602 product, POMINO v2. This new release will contain a few additional updates, including
603 but not limited to using MODIS Collection 6 Merged 10-km Level-2 AOD data that
604 combine the Dark Target (Levy et al., 2013) and Deep Blue (Sayer et al., 2014) products,
605 as well as MODIS MCD43C2 Collection 6 daily BRDF data. Meanwhile, the POMINO

606 algorithm framework is being applied to the recently launched TropOMI instrument
607 that provides NO_2 information at a much higher spatial resolution (3.5 x 7 km^2). A
608 modified algorithm can also be used to retrieve sulfur dioxide, formaldehyde and other
609 trace gases from TropOMI, for which purposes our algorithm will be available to the
610 community on a collaborative basis. Future research can correct the SSA and NO_2
611 vertical profile to further improve the retrieval algorithm, and can use more
612 comprehensive independent data to evaluate the resulting satellite products.

613 **Acknowledgements**

614 This research is supported by the National Natural Science Foundation of China
615 (41775115), the 973 program (2014CB441303), the Chinese Scholarship Council, and
616 the EU FP7 QA4ECV project (grant no. 607405).

617 **Appendix A: Introduction to the QA4ECV product**

618 The QA4ECV NO_2 product (http://www.qa4ecv.eu/) builds on a (EU-) consortium
619 approach to retrieve NO_2 from GOME, SCIAMACHY, GOME-2, and OMI. The main
620 contributions are provided by BIRA-IASB, the University of Bremen (IUP), MPIC,
621 KNMI, and Wageningen University. Uncertainties in spectral fitting for NO_2 SCDs and
622 in AMF calculations were evaluated by Zara et al. (2018) and Lorente et al. (2017),
623 respectively. QA4ECV contains improved SCD NO_2 data (Zara et al., 2018). Lorente
624 et al., (2017) showed that across the above algorithms, there a structural uncertainty by
625 42% in the NO_2 AMF calculation over polluted areas. By comparing to our POMINO
626 product, Lorente et al. also showed that the choice of aerosol correction may introduce
627 an additional uncertainty by up to 50% for situations with high polluted cases,
628 consistent with Lin et al. (2014b, 2015) and the findings here. For a complete
629 description of the QA4ECV algorithm improvements, and quality assurance, please see
630 Boersma et al. (2018).

Appendix B: Constructing the CALIOP monthly climatology of aerosol extinction vertical profile

Our use the all-sky Level-2 CALIOP data to construct the Level-3 monthly climatology. We choose the all-sky product instead of clear-sky data, since previous studies indicate that the climatological aerosol extinction profiles are affected insignificantly by the presence of clouds (Koffi et al., 2012; Winker et al., 2013). As we use this climatological data to adjust GEOS-Chem results, choosing all-sky data improves consistency with the model simulation when doing the daily correction.

To select valid pixels, we follow the data quality criteria by Winker et al., (2013) and Amiridis et al., (2015). Only the pixels with Cloud Aerosol Discrimination (CAD) scores between -20 and -100 with extinction Quality Control (QC) flag valued at 0, 1, 18, and 16 are selected. We further discard samples with an extinction uncertainty of 99.9 km^{-1}, which is indicative of unreliable retrieval. We only accept extinction values falling in the range from 0.0 to 1.25, according to CALIOP observation thresholds. Previous studies showed that weakly scattering edges of icy clouds are sometimes misclassified as aerosols (Winker et al., 2013). To eliminate contamination from icy clouds we exclude the aerosol layers above the cloud layer (with layer-top temperature below 0 ℃) when both of them are above 4km (Winker et al., 2013).

After the pixel-based screening, we aggregate the CALIOP data at the model grid (0.667° long. x 0.5° lat.) and vertical resolution (47 layers, with 36 layers or so in the troposphere). For each grid cell, we choose the CALIOP pixels within 1.5° of the grid cell center. CALIOP Level-2 data are always presented at the fixed 399 altitudes above sea level. To account for the difference in surface elevation between a CALIOP pixel and the respective model grid cell, we convert the altitude of the pixel to a height above the ground, by using the surface elevation data provided in CALIOP. We then average horizontally and vertically the profiles of all pixels within one model grid cell and layer.

We do the regridding day-by-day for all grid cells to ensure that GEOS-Chem and CALIOP extinction profiles are coincident spatially and temporally. Finally, we compile a monthly climatological dataset by averaging over 2007–2015.

Figure A1 shows the number of aerosol extinction profiles in each grid cell and 12 x 9 = 108 months that are used to compile the CALIOP climatology, both before and after data screening. Table A1 presents additional information on monthly and yearly bases. On average, there are 165 and 47 aerosol extinction profiles per month per grid cell before and after screening, respectively. In the final 9-year monthly climatology, each grid cell has about 420 aerosol extinction profiles on average, about 28% of the prior-screening profiles. Figure A1 shows that the number of valid profiles decreases sharply over the Tibet Plateau and at higher latitudes (> 43 $^\circ$ N) due to complex terrain and icy/snowy ground.

As discussed above, we choose the CALIOP pixels within 1.5° of a grid cell center. We test this choice by examining the aerosol layer height (ALH) produced for that grid cell. The ALH is defined as the extinction-weighted height of aerosols (see Eq. A1, where n denotes the number of tropospheric layers, ε_i the aerosol extinction at layer i, and H_i the layer center height above the ground). We find that choosing pixels within 1.0° of a grid cell center leads to a nosier horizontal distribution of ALH, owing to the small footprint of CALIOP. On the other hand, choosing 2.0° leads to a too smooth spatial gradient of ALH with local characteristics of aerosol vertical distributions are largely lost. We thus decide that 1.5 $^\circ$ is a good balance between noise and smoothness.

$$\mathrm{ALH} = \frac{\sum_{i=1}^{i=n} \varepsilon_i \mathrm{H}_i}{\sum_{i=1}^{i=n} \varepsilon_i} \qquad \text{(A1)}$$

Certain grid cells do not contain sufficient valid observations for some months of the climatological dataset. We fill in missing monthly values of a grid cell using valid data

682 in the surrounding 5 x 5 = 25 grid cells (within ~ 100 km). If the 25 grid cells do not
683 have enough valid data, we use those in the surrounding 7 x 7 = 49 grid cells (within ~
684 150 km). A similar procedure is used by Lin et al. (2014b, 2015) to fill in missing values
685 in the gridded MODIS AOD dataset.

686 For each grid cell in each month, we further correct singular values in the vertical profile.
687 In a month, if a grid cell *i* has an ALH outside mean $\pm 1\ \sigma$ of its surrounding 25 or 49
688 grid cells, we select *i*'s surrounding grid cell *j* whose ALH is the median of *i*'s
689 surrounding grid cells, and use *j*'s profile to replace *i*'s. Whether 25 or 49 surrounding
690 grid cells are chosen depends on the number of valid pixels shown in Fig. A1b. If the
691 number of valid pixels in *i* is below mean–1 σ of all grid cells in the whole domain,
692 which is often the case for Tibetan grid cells, we use *i*'s surrounding 49 grid cells;
693 otherwise we use *i*'s surrounding 25 grid cells.

694 **Appendix C. Comparing our and NASA's CALIOP monthly climatology**

695 We compare our gridded climatological profiles to NASA CALIOP Version 3 Level-3
696 all-sky monthly profiles at 532 nm (Winker et al., 2013). The NASA Level-3 data has
697 a horizontal resolution of 2° lat. $\times 5^\circ$ lon. and a vertical resolution of 60 m (from -
698 0.5 to 12 km above sea level). We combine NASA monthly data over 2007–2015 to
699 construct a monthly climatology for comparison with our own compilation. We only
700 choose aerosol extinction data in the troposphere with error less than 0.15 (the valid
701 range given in the CALIOP dataset). If the number of valid monthly profiles in a grid
702 cell is less than five (i.e., for the same month in five out of the nine years), then we
703 exclude data in that grid cell; see the dark gray grid cells in Fig. 2c.

704 Several methodological differences exist between generating our and NASA CALIOP
705 datasets. First, the two datasets have different horizontal resolutions. Also, we sample
706 all valid CALIOP pixels within 1.5° of a grid cell center, whereas the NASA dataset

samples all valid pixels within a grid cell. Besides, our CALIOP dataset involves several steps of horizontal interpolation, for purposes of subsequent cloud and NO_2 retrievals, which is not done in the NASA dataset. In addition, we match CALIOP data vertically to the GEOS-Chem vertical resolution, whereas the NASA dataset maintains the original resolution.

Figure 2c shows the spatial distribution of ALH in all seasons based on NASA CALIOP Level-3 all-sky monthly climatology. The horizontal resolution of NASA data is much coarser than ours; and NASA data are largely missing over the southwest with complex terrains. We choose to focus on the comparison over East China (the black box in Fig. 1a). Over East China, the two climatology datasets generally exhibit similar spatial patterns of ALH in all seasons (Fig. 2a, c). The NASA dataset suggests higher ALHs than ours over Eastern China, especially in summer, due mainly to differences in the sampling and regridding processes. Figure 3c further compares the monthly variation of ALH between our (black line with error bars) and NASA (blue filled triangles) datasets averaged over East China. The two datasets are consistent in almost all months, indicating that their regional differences are largely smoothed out by spatial averaging.

References

Acarreta, J. R., De Haan, J. F. and Stammes, P.: Cloud pressure retrieval using the O_2 -O_2 absorption band at 477 nm, J. Geophys. Res., 109(D5), D05204, doi:10.1029/2003JD003915, 2004.

Amiridis, V., Marinou, E., Tsekeri, A., Wandinger, U., Schwarz, A., Giannakaki, E., Mamouri, R., Kokkalis, P., Binietoglou, I., Solomos, S., Herekakis, T., Kazadzis, S., Gerasopoulos, E., Proestakis, E., Kottas, M., Balis, D., Papayannis, A., Kontoes, C., Kourtidis, K., Papagiannopoulos, N., Mona, L., Pappalardo, G., Le Rille, O. and Ansmann, A.: LIVAS: a 3-D multi-wavelength aerosol/cloud database based on

732 CALIPSO and EARLINET, Atmos. Chem. Phys., 15(13), 7127–7153,
733 doi:10.5194/acp-15-7127-2015, 2015.

734 Belmonte Rivas, M., Veefkind, P., Boersma, F., Levelt, P., Eskes, H. and Gille, J.:
735 Intercomparison of daytime stratospheric NO_2 satellite retrievals and model
736 simulations, Atmos. Meas. Tech., 7(7), 2203–2225, doi:10.5194/amt-7-2203-2014,
737 2014.

738 Boersma, K. F., Eskes, H. J. and Brinksma, E. J.: Error analysis for tropospheric NO_2
739 retrieval from space, J. Geophys. Res. Atmos., 109(D4), n/a-n/a,
740 doi:10.1029/2003JD003962, 2004.

741 Boersma, K. F., Eskes, H. J., Veefkind, J. P., Brinksma, E. J., van der A, R. J., Sneep,
742 M., van den Oord, G. H. J., Levelt, P. F., Stammes, P., Gleason, J. F. and Bucsela, E.
743 J.: Near-real time retrieval of tropospheric NO_2 from OMI, Atmos. Chem. Phys., 7(8),
744 2103–2118, doi:10.5194/acp-7-2103-2007, 2007.

745 Boersma, K. F., Eskes, H. J., Dirksen, R. J., van der A, R. J., Veefkind, J. P.,
746 Stammes, P., Huijnen, V., Kleipool, Q. L., Sneep, M., Claas, J., Leitão, J., Richter, A.,
747 Zhou, Y. and Brunner, D.: An improved tropospheric NO_2 column retrieval algorithm
748 for the Ozone Monitoring Instrument, Atmos. Meas. Tech., 4(9), 1905–1928,
749 doi:10.5194/amt-4-1905-2011, 2011.

750 Boersma, K.F., Eskes, H. J., Richter, A., De Smedt, I., Lorente, A., Beirle, S., van
751 Geffen, J. H. G. M., Zara, M., Peters, E., Van Roozendael, M., Wagner, T., Maasakkers,
752 J. D., van der A, R. J., Nightingale, J., De Rudder, A., Irie, H., and Pinardi, G.:
753 Improving algorithms and uncertainty estimates for satellite NO_2 retrievals: Results
754 from the Quality Assurance for Essential Climate Variables (QA4ECV) project, amt-
755 2018-200, submitted, 2018.

Bucsela, E. J., Celarier, E. A., Wenig, M. O., Gleason, J. F., Veefkind, J. P., Boersma, K. F. and Brinksma, E. J.: Algorithm for NO_2 vertical column retrieval from the ozone monitoring instrument, IEEE Trans. Geosci. Remote Sens., 44(5), 1245–1258, doi:10.1109/TGRS.2005.863715, 2006.

Bucsela, E. J., Krotkov, N. A., Celarier, E. A., Lamsal, L. N., Swartz, W. H., Bhartia, P. K., Boersma, K. F., Veefkind, J. P., Gleason, J. F. and Pickering, K. E.: A new stratospheric and tropospheric NO_2 retrieval algorithm for nadir-viewing satellite instruments: applications to OMI, Atmos. Meas. Tech., 6(10), 2607–2626, doi:10.5194/amt-6-2607-2013, 2013.

Castellanos, P., Boersma, K. F. and van der Werf, G. R.: Satellite observations indicate substantial spatiotemporal variability in biomass burning NO_X emission factors for South America, Atmos. Chem. Phys., 14(8), 3929–3943, doi:10.5194/acp-14-3929-2014, 2014.

Castellanos, P., Boersma, K. F., Torres, O. and de Haan, J. F.: OMI tropospheric NO_2 air mass factors over South America: effects of biomass burning aerosols, Atmos. Meas. Tech., 8(9), 3831–3849, doi:10.5194/amt-8-3831-2015, 2015.

Chazette, P., Raut, J.-C., Dulac, F., Berthier, S., Kim, S.-W., Royer, P., Sanak, J., Loaëc, S. and Grigaut-Desbrosses, H.: Simultaneous observations of lower tropospheric continental aerosols with a ground-based, an airborne, and the spaceborne CALIOP lidar system, J. Geophys. Res., 115(D4), D00H31, doi:10.1029/2009JD012341, 2010.

Chimot, J., Vlemmix, T., Veefkind, J. P., de Haan, J. F. and Levelt, P. F.: Impact of aerosols on the OMI tropospheric NO_2 retrievals over industrialized regions: how accurate is the aerosol correction of cloud-free scenes via a simple cloud model?, Atmos. Meas. Tech., 9(2), 359–382, doi:10.5194/amt-9-359-2016, 2016.

781 Clémer, K., Van Roozendael, M., Fayt, C., Hendrick, F., Hermans, C., Pinardi, G.,
782 Spurr, R., Wang, P. and De Mazière, M.: Multiple wavelength retrieval of
783 tropospheric aerosol optical properties from MAX-DOAS measurements in Beijing,
784 Atmos. Meas. Tech., 3(4), 863–878, doi:10.5194/amt-3-863-2010, 2010.

785 Cui, Y., Lin, J., Song, C., Liu, M., Yan, Y., Xu, Y. and Huang, B.: Rapid growth in
786 nitrogen dioxide pollution over Western China, 2005–2013, Atmos. Chem. Phys.,
787 16(10), 6207–6221, doi:10.5194/acp-16-6207-2016, 2016.

788 Dirksen, R. J., Boersma, K. F., Eskes, H. J., Ionov, D. V., Bucsela, E. J., Levelt, P. F.
789 and Kelder, H. M.: Evaluation of stratospheric NO_2 retrieved from the Ozone
790 Monitoring Instrument: Intercomparison, diurnal cycle, and trending, J. Geophys.
791 Res., 116(D8), D08305, doi:10.1029/2010JD014943, 2011.

792 van Geffen, J. H. G. M., Boersma, K. F., Van Roozendael, M., Hendrick, F., Mahieu,
793 E., De Smedt, I., Sneep, M. and Veefkind, J. P.: Improved spectral fitting of nitrogen
794 dioxide from OMI in the 405–465 nm window, Atmos. Meas. Tech., 8(4), 1685–
795 1699, doi:10.5194/amt-8-1685-2015, 2015.

796 Gielen, C., Van Roozendael, M., Hendrick, F., Pinardi, G., Vlemmix, T., De Bock,
797 V., De Backer, H., Fayt, C., Hermans, C., Gillotay, D. and Wang, P.: A simple and
798 versatile cloud-screening method for MAX-DOAS retrievals, Atmos. Meas. Tech.,
799 7(10), 3509–3527, doi:10.5194/amt-7-3509-2014, 2014.

800 Hendrick, F., Muller, J. F., Clemer, K., Wang, P., De Maziere, M., Fayt, C., Gielen,
801 C., Hermans, C., Ma, J. Z., Pinardi, G., Stavrakou, T., Vlemmix, T., and Van
802 Roozendael, M.: Four years of ground-based MAX-DOAS observations of HONO
803 and NO_2 in the Beijing area, Atmospheric Chemistry and Physics, 14, 765-781,
804 10.5194/acp-14-765-2014, 2014.

805 Huang, Z., Huang, J., Bi, J., Wang, G., Wang, W., Fu, Q., Li, Z., Tsay, S.-C. and Shi,
806 J.: Dust aerosol vertical structure measurements using three MPL lidars during 2008
807 China-U.S. joint dust field experiment, J. Geophys. Res. Atmos., 115(D7), n/a-n/a,
808 doi:10.1029/2009JD013273, 2010.

809 Irie, H., Boersma, K. F., Kanaya, Y., Takashima, H., Pan, X. and Wang, Z. F.:
810 Quantitative bias estimates for tropospheric NO_2 columns retrieved from
811 SCIAMACHY, OMI, and GOME-2 using a common standard for East Asia, Atmos.
812 Meas. Tech., 5(10), 2403–2411, doi:10.5194/amt-5-2403-2012, 2012.

813 Jethva, H., Torres, O., and Ahn, C.: A ten-year global record of absorbing aerosols
814 above clouds from OMI's near-UV observations, in: Remote Sensing of the Atmosphere,
815 Clouds, and Precipitation Vi, edited by: Im, E., Kumar, R., and Yang, S., Proceedings
816 of SPIE, 2016.

817 Johnson, M. S., Meskhidze, N. and Praju Kiliyanpilakkil, V.: A global comparison of
818 GEOS-Chem-predicted and remotely-sensed mineral dust aerosol optical depth and
819 extinction profiles, J. Adv. Model. Earth Syst., 4(3), M07001,
820 doi:10.1029/2011MS000109, 2012.

821 Kacenelenbogen, M., Redemann, J., Vaughan, M. A., Omar, A. H., Russell, P. B.,
822 Burton, S., Rogers, R. R., Ferrare, R. A. and Hostetler, C. A.: An evaluation of
823 CALIOP/CALIPSO's aerosol-above-cloud detection and retrieval capability over
824 North America, J. Geophys. Res. Atmos., 119(1), 230–244,
825 doi:10.1002/2013JD020178, 2014.

826 Kanaya, Y., Irie, H., Takashima, H., Iwabuchi, H., Akimoto, H., Sudo, K., Gu, M.,
827 Chong, J., Kim, Y. J., Lee, H., Li, A., Si, F., Xu, J., Xie, P.-H., Liu, W.-Q., Dzhola,
828 A., Postylyakov, O., Ivanov, V., Grechko, E., Terpugova, S. and Panchenko, M.:
829 Long-term MAX-DOAS network observations of NO_2 in Russia and Asia

(MADRAS) during the period 2007-2012: instrumentation, elucidation of climatology, and comparisons with OMI satellite observations and global model simulations, Atmos. Chem. Phys., 14(15), 7909–7927, doi:10.5194/acp-14-7909-2014, 2014.

Kim, S.-W., Heckel, A., Frost, G. J., Richter, A., Gleason, J., Burrows, J. P., McKeen, S., Hsie, E.-Y., Granier, C. and Trainer, M.: NO_2 columns in the western United States observed from space and simulated by a regional chemistry model and their implications for NO_x emissions, J. Geophys. Res., 114(D11), D11301, doi:10.1029/2008JD011343, 2009.

Koffi, B., Schulz, M., Bréon, F.-M., Griesfeller, J., Winker, D., Balkanski, Y., Bauer, S., Berntsen, T., Chin, M., Collins, W. D., Dentener, F., Diehl, T., Easter, R., Ghan, S., Ginoux, P., Gong, S., Horowitz, L. W., Iversen, T., Kirkevåg, A., Koch, D., Krol, M., Myhre, G., Stier, P. and Takemura, T.: Application of the CALIOP layer product to evaluate the vertical distribution of aerosols estimated by global models: AeroCom phase I results, J. Geophys. Res. Atmos., 117(D10), n/a-n/a, doi:10.1029/2011JD016858, 2012.

Leitão, J., Richter, A., Vrekoussis, M., Kokhanovsky, A., Zhang, Q. J., Beekmann, M. and Burrows, J. P.: On the improvement of NO_2 satellite retrievals – aerosol impact on the airmass factors, Atmos. Meas. Tech., 3(2), 475–493, doi:10.5194/amt-3-475-2010, 2010.

Lerot, C., Stavrakou, T., De Smedt, I., Müller, J.-F. and Van Roozendael, M.: Glyoxal vertical columns from GOME-2 backscattered light measurements and comparisons with a global model, Atmos. Chem. Phys., 10(24), 12059–12072, doi:10.5194/acp-10-12059-2010, 2010.

Levy, R. C., Mattoo, S., Munchak, L. A., Remer, L. A., Sayer, A. M., Patadia, F. and Hsu, N. C.: The Collection 6 MODIS aerosol products over land and ocean, Atmos. Meas. Tech., 6(11), 2989–3034, doi:10.5194/amt-6-2989-2013, 2013.

Li, S., Yu, C., Chen, L., Tao, J., Letu, H., Ge, W., Si, Y. and Liu, Y.: Inter-comparison of model-simulated and satellite-retrieved componential aerosol optical depths in China, Atmos. Environ., 141, 320–332, doi:https://doi.org/10.1016/j.atmosenv.2016.06.075, 2016.

Lin, J., Pan, D., Davis, S. J., Zhang, Q., He, K., Wang, C., Streets, D. G., Wuebbles, D. J. and Guan, D.: China's international trade and air pollution in the United States, Proc. Natl. Acad. Sci., 111(5), 1736–1741, doi:10.1073/pnas.1312860111, 2014a.

Lin, J.-T.: Satellite constraint for emissions of nitrogen oxides from anthropogenic, lightning and soil sources over East China on a high-resolution grid, Atmos. Chem. Phys., 12(6), 2881–2898, doi:10.5194/acp-12-2881-2012, 2012.

Lin, J.-T., McElroy, M. B. and Boersma, K. F.: Constraint of anthropogenic NO_X emissions in China from different sectors: a new methodology using multiple satellite retrievals, Atmos. Chem. Phys., 10(1), 63–78, doi:10.5194/acp-10-63-2010, 2010.

Lin, J.-T., Martin, R. V., Boersma, K. F., Sneep, M., Stammes, P., Spurr, R., Wang, P., Van Roozendael, M., Clémer, K. and Irie, H.: Retrieving tropospheric nitrogen dioxide from the Ozone Monitoring Instrument: effects of aerosols, surface reflectance anisotropy, and vertical profile of nitrogen dioxide, Atmos. Chem. Phys., 14(3), 1441–1461, doi:10.5194/acp-14-1441-2014, 2014b.

Lin, J.-T., Liu, M.-Y., Xin, J.-Y., Boersma, K. F., Spurr, R., Martin, R. and Zhang, Q.: Influence of aerosols and surface reflectance on satellite NO_2 retrieval: seasonal and spatial characteristics and implications for NO_x emission constraints, Atmos. Chem. Phys., 15(19), 11217–11241, doi:10.5194/acp-15-11217-2015, 2015.

879 Lorente, A., Folkert Boersma, K., Yu, H., Dörner, S., Hilboll, A., Richter, A., Liu, M.,
880 Lamsal, L. N., Barkley, M., De Smedt, I., Van Roozendael, M., Wang, Y., Wagner,
881 T., Beirle, S., Lin, J.-T., Krotkov, N., Stammes, P., Wang, P., Eskes, H. J. and Krol,
882 M.: Structural uncertainty in air mass factor calculation for NO_2 and HCHO satellite
883 retrievals, Atmos. Meas. Tech., 10(3), 759–782, doi:10.5194/amt-10-759-2017, 2017.

884 Lucht, W., Schaaf, C. B. and Strahler, A. H.: An algorithm for the retrieval of albedo
885 from space using semiempirical BRDF models, IEEE Trans. Geosci. Remote Sens.,
886 38(2), 977–998, doi:10.1109/36.841980, 2000.

887 Ma, J. Z., Beirle, S., Jin, J. L., Shaiganfar, R., Yan, P. and Wagner, T.: Tropospheric
888 NO_2 vertical column densities over Beijing: results of the first three years of ground-
889 based MAX-DOAS measurements (2008-2011) and satellite validation, Atmos.
890 Chem. Phys., 13(3), 1547–1567, doi:10.5194/acp-13-1547-2013, 2013.

891 Ma, X. and Yu, F.: Seasonal variability of aerosol vertical profiles over east US and
892 west Europe: GEOS-Chem/APM simulation and comparison with CALIPSO
893 observations, Atmos. Res., 140–141, 28–37,
894 doi:https://doi.org/10.1016/j.atmosres.2014.01.001, 2014.

895 Martin, R. V.: An improved retrieval of tropospheric nitrogen dioxide from GOME, J.
896 Geophys. Res., 107(D20), 4437, doi:10.1029/2001JD001027, 2002.

897 Misra, A., Tripathi, S. N., Kaul, D. S. and Welton, E. J.: Study of MPLNET-Derived
898 Aerosol Climatology over Kanpur, India, and Validation of CALIPSO Level 2
899 Version 3 Backscatter and Extinction Products, J. Atmos. Ocean. Technol., 29(9),
900 1285–1294, doi:10.1175/JTECH-D-11-00162.1, 2012.

901 Miyazaki, K. and Eskes, H.: Constraints on surface NO_X emissions by assimilating
902 satellite observations of multiple species, Geophys. Res. Lett., 40(17), 4745–4750,
903 doi:10.1002/grl.50894, 2013.

Proestakis, E., Amiridis, V., Marinou, E., Georgoulias, A. K., Solomos, S., Kazadzis, S., Chimot, J., Che, H., Alexandri, G., Binietoglou, I., Kourtidis, K. A., de Leeuw, G. and van der A, R. J.: 9-year spatial and temporal evolution of desert dust aerosols over South-East Asia as revealed by CALIOP, Atmos. Chem. Phys. Discuss., 1–35, doi:10.5194/acp-2017-797, 2017.

Richter, A., Begoin, M., Hilboll, A. and Burrows, J. P.: An improved NO_2 retrieval for the GOME-2 satellite instrument, Atmos. Meas. Tech., 4(6), 1147–1159, doi:10.5194/amt-4-1147-2011, 2011.

Marchenko, S., Krotkov, N. A., Lamsal, L. N., Celarier, E. A., Swartz, W. H., and Bucsela, E. J.: Revising the slant column density retrieval of nitrogen dioxide observed by the Ozone Monitoring Instrument, J. Geophys. Res. Atmos., 120(11), 5670–5692, doi:10.1002/2014JD022913, 2015.

Sareen, N., Schwier, A. N., Shapiro, E. L., Mitroo, D. and McNeill, V. F.: Secondary organic material formed by methylglyoxal in aqueous aerosol mimics, Atmos. Chem. Phys., 10(3), 997–1016, doi:10.5194/acp-10-997-2010, 2010.

Sayer, A. M., Munchak, L. A., Hsu, N. C., Levy, R. C., Bettenhausen, C. and Jeong, M.-J.: MODIS Collection 6 aerosol products: Comparison between Aqua's e-Deep Blue, Dark Target, and "merged" data sets, and usage recommendations, J. Geophys. Res. Atmos., 119(24), 13,965-13,989, doi:10.1002/2014JD022453, 2014.

Schenkeveld, V. M. E., Jaross, G., Marchenko, S., Haffner, D., Kleipool, Q. L., Rozemeijer, N. C., Veefkind, J. P., and Levelt, P. F.: In-flight performance of the Ozone Monitoring Instrument, Atmospheric Measurement Techniques, 10, 1957-1986, 10.5194/amt-10-1957-2017, 2017.

Stammes, P., Sneep, M., de Haan, J. F., Veefkind, J. P., Wang, P. and Levelt, P. F.: Effective cloud fractions from the Ozone Monitoring Instrument: Theoretical

framework and validation, J. Geophys. Res., 113(D16), D16S38, doi:10.1029/2007JD008820, 2008.

Stavrakou, T., Müller, J.-F., Bauwens, M., De Smedt, I., Lerot, C., Van Roozendael, M., Coheur, P.-F., Clerbaux, C., Boersma, K. F., van der A, R. and Song, Y.: Substantial Underestimation of Post-Harvest Burning Emissions in the North China Plain Revealed by Multi-Species Space Observations, Sci. Rep., 6, 32307, doi:10.1038/srep32307, 2016.

van Donkelaar, A., Martin, R. V., Spurr, R. J. D., Drury, E., Remer, L. A., Levy, R. C., and Wang, J.: Optimal estimation for global ground-level fine particulate matter concentrations, Journal of Geophysical Research-Atmospheres, 118, 5621-5636, 10.1002/jgrd.50479, 2013.

Veefkind, J. P., de Haan, J. F., Sneep, M. and Levelt, P. F.: Improvements to the OMI O_2-O_2 operational cloud algorithm and comparisons with ground-based radar–lidar observations, Atmos. Meas. Tech., 9(12), 6035–6049, doi:10.5194/amt-9-6035-2016, 2016.

Verstraeten, W. W., Neu, J. L., Williams, J. E., Bowman, K. W., Worden, J. R. and Boersma, K. F.: Rapid increases in tropospheric ozone production and export from China, Nat. Geosci., 8, 690 [online] Available from: http://dx.doi.org/10.1038/ngeo2493, 2015.

Wang, J., Jacob, D. J. and Martin, S. T.: Sensitivity of sulfate direct climate forcing to the hysteresis of particle phase transitions, J. Geophys. Res. Atmos., 113(D11), n/a-n/a, doi:10.1029/2007JD009368, 2008a.

Wang, M., Gu, J., Yang, R., Zeng, L. and Wang, S.: Comparison of cloud type and frequency over China from surface, FY-2E, and CloudSat observations, vol. 9259, pp.

925913–925914. [online] Available from: http://dx.doi.org/10.1117/12.2069110, 2014.

Wang, P. and Stammes, P.: Evaluation of SCIAMACHY Oxygen A band cloud heights using Cloudnet measurements, Atmos. Meas. Tech., 7(5), 1331–1350, doi:10.5194/amt-7-1331-2014, 2014.

Wang, P., Stammes, P., van der A, R., Pinardi, G. and van Roozendael, M.: FRESCO+: an improved O_2 A-band cloud retrieval algorithm for tropospheric trace gas retrievals, Atmos. Chem. Phys., 8(21), 6565–6576, doi:10.5194/acp-8-6565-2008, 2008b.

Wang, X., Huang, J., Zhang, R., Chen, B. and Bi, J.: Surface measurements of aerosol properties over northwest China during ARM China 2008 deployment, J. Geophys. Res. Atmos., 115(D7), n/a-n/a, doi:10.1029/2009JD013467, 2010.

Wang, Y., Penning de Vries, M., Xie, P. H., Beirle, S., Dörner, S., Remmers, J., Li, A. and Wagner, T.: Cloud and aerosol classification for 2.5 years of MAX-DOAS observations in Wuxi (China) and comparison to independent data sets, Atmos. Meas. Tech., 8(12), 5133–5156, doi:10.5194/amt-8-5133-2015, 2015.

Wang, Y., Lampel, J., Xie, P., Beirle, S., Li, A., Wu, D. and Wagner, T.: Ground-based MAX-DOAS observations of tropospheric aerosols, NO_2, SO_2 and HCHO in Wuxi, China, from 2011 to 2014, Atmos. Chem. Phys., 17(3), 2189–2215, doi:10.5194/acp-17-2189-2017, 2017a.

Wang, Y., Beirle, S., Lampel, J., Koukouli, M., De Smedt, I., Theys, N., Li, A., Wu, D., Xie, P., Liu, C., Van Roozendael, M., Stavrakou, T., Müller, J.-F. and Wagner, T.: Validation of OMI, GOME-2A and GOME-2B tropospheric NO_2, SO_2 and HCHO products using MAX-DOAS observations from 2011 to 2014 in Wuxi, China:

977 investigation of the effects of priori profiles and aerosols on the satellite products,
978 Atmos. Chem. Phys., 17(8), 5007–5033, doi:10.5194/acp-17-5007-2017, 2017b.

979 Winker, D. M., Pelon, J., Coakley, J. A., Ackerman, S. A., Charlson, R. J., Colarco, P.
980 R., Flamant, P., Fu, Q., Hoff, R. M., Kittaka, C., Kubar, T. L., Le Treut, H.,
981 Mccormick, M. P., Mégie, G., Poole, L., Powell, K., Trepte, C., Vaughan, M. A. and
982 Wielicki, B. A.: The CALIPSO Mission, Bull. Am. Meteorol. Soc., 91(9), 1211–
983 1230, doi:10.1175/2010BAMS3009.1, 2010.

984 Winker, D. M., Tackett, J. L., Getzewich, B. J., Liu, Z., Vaughan, M. A. and Rogers,
985 R. R.: The global 3-D distribution of tropospheric aerosols as characterized by
986 CALIOP, Atmos. Chem. Phys., 13(6), 3345–3361, doi:10.5194/acp-13-3345-2013,
987 2013.

988 Zara, M., Boersma, K. F., De Smedt, I., Richter, A., Peters, E., Van Geffen, J. H. G.
989 M., Beirle, S., Wagner, T., Van Roozendael, M., Marchenko, S., Lamsal, L. N. and
990 Eskes, H. J.: Improved slant column density retrieval of nitrogen dioxide and
991 formaldehyde for OMI and GOME-2A from QA4ECV: intercomparison, uncertainty
992 characterization, and trends, Atmos. Meas. Tech. Discuss., 1–47, doi:10.5194/amt-
993 2017-453, 2018.

994 Zhang, Q., Streets, D. G., Carmichael, G. R., He, K. B., Huo, H., Kannari, A.,
995 Klimont, Z., Park, I. S., Reddy, S., Fu, J. S., Chen, D., Duan, L., Lei, Y., Wang, L. T.
996 and Yao, Z. L.: Asian emissions in 2006 for the NASA INTEX-B mission, Atmos.
997 Chem. Phys., 9(14), 5131–5153, doi:10.5194/acp-9-5131-2009, 2009.

998 Zhao, C. and Wang, Y.: Assimilated inversion of NO_X emissions over east Asia using
999 OMI NO_2 column measurements, Geophys. Res. Lett., 36(6), L06805,
1000 doi:10.1029/2008GL037123, 2009.

1001 Zhao, H. Y., Zhang, Q., Guan, D. B., Davis, S. J., Liu, Z., Huo, H., Lin, J. T., Liu, W.
1002 D. and He, K. B.: Assessment of China's virtual air pollution transport embodied in
1003 trade by using a consumption-based emission inventory, Atmos. Chem. Phys., 15(10),
1004 5443–5456, doi:10.5194/acp-15-5443-2015, 2015.

1005 Zhou, Y., Brunner, D., Spurr, R. J. D., Boersma, K. F., Sneep, M., Popp, C. and
1006 Buchmann, B.: Accounting for surface reflectance anisotropy in satellite retrievals of
1007 tropospheric NO_2, Atmos. Meas. Tech., 3(5), 1185–1203, doi:10.5194/amt-3-1185-
1008 2010, 2010.

1009 Zhu, W., Xu, C., Qian, X. and Wei, H.: Statistical analysis of the spatial-temporal
1010 distribution of aerosol extinction retrieved by micro-pulse lidar in Kashgar, China,
1011 Opt. Express, 21(3), 2531–2537, doi:10.1364/OE.21.002531, 2013.

1012

1013

Table A1. Number of CALIOP observations in a grid cell (0.667°× 0.5°).

	Before filtering				After filtering			
	Mean	Median	Minima	Maximum	Mean	Median	Minima	Maximum
For a month	165	169	0	291	47	39	0	223
For the same month in nine years	1483	1513	192	1921	420	395	0	1548
For all months in nine years	17794	18528	5608	20781	5033	5381	146	12650

1014

Table 1. MAX-DOAS measurement sites and corresponding meteorological stations.

MAX-DOAS site name	Site information	Measurement times	Corresponding meteorological station name	Meteorological station information
Xianghe	116.96°E, 39.75°N, 36 m, suburban	2012/01/01 -2012/12/31	CAPITAL INTERNATIONA	116.89°E, 40.01°N, 35.4 m
IAP	116.38°E, 39.98°N, 92 m, urban	2008/06/22 -2009/04/16	CAPITAL INTERNATIONA	116.89°E, 40.01°N, 35.4 m
Wuxi	120.31°E, 31.57°N, 20 m, urban	2012/01/01 -2012/12/31	HONGQIAO INTL	121.34°E, 31.20°N, 3 m

1015

Table 2. Evaluation of OMI NO_2 products with respect to MAX-DOAS on 27 haze days [1].

	POMINO v1.1	POMINO	DOMINO v2	QA4ECV
Slope	1.07	0.80	1.11	0.58
Intercept (10^{15} molec./cm^2)	-3.58	1.76	-11.79	3.20
R^2	0.76	0.68	0.38	0.34
NMB (%)	4.4	-9.4	-5.0	-26.11

1. The haze days are determined when the ground meteorological station data and MODIS/Aqua corrected reflectance (true color) data both indicate a haze day. Average across the days, AOD = 1.13 (median = 1.10), SSA = 0.90 (0.91), MAX-DOAS NO_2 = 51.92 x 10^{15} molec. cm^{-2}, and CF = 0.06 (0.03).

Table 3. Evaluation of OMI NO_2 products with respect to MAX-DOAS on 36 cloud-free days [1].

	POMINO v1.1	POMINO	DOMINO v2	QA4ECV
Slope	1.30	1.13	0.92	0.79
Intercept	-0.61	0.31	2.32	1.05
R^2	0.55	0.56	0.53	0.63
NMB (%)	29.4	20.8	21.9	-5.83

1. CF=0 in POMINO product. Average across the days, AOD = 0.60 (median = 0.47), SSA = 0.90 (0.91), and MAX-DOAS $NO_2 = 26.82 \times 10^{15}$ molec. cm^{-2}.

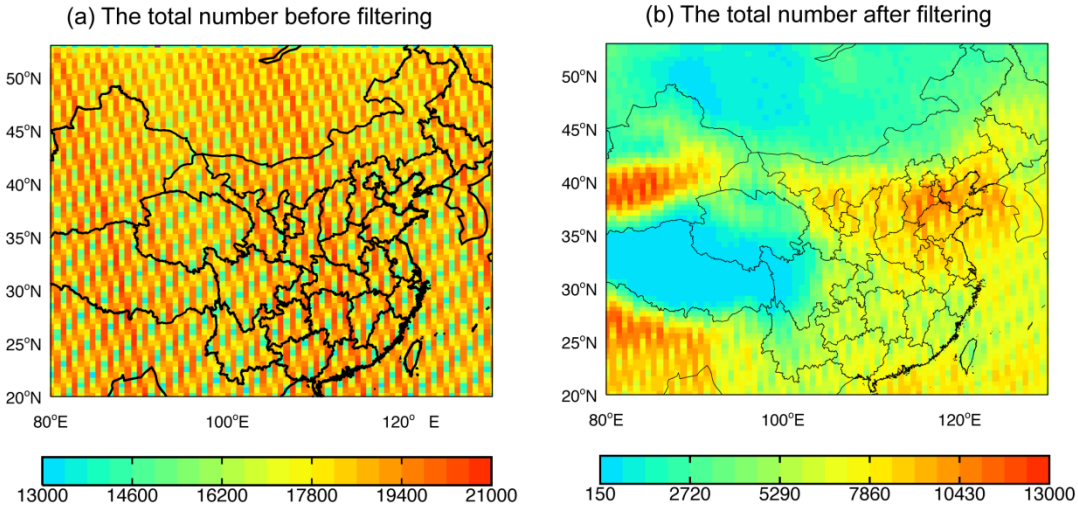

1022 Figure A1. The total number of CALIOP Level-2 aerosol extinction profiles at 532 nm
1023 used to derive our climatological (2007–2015) dataset on a 0.667° long. x 0.5° lat. grid
1024 (a) before and (b) after filtering.

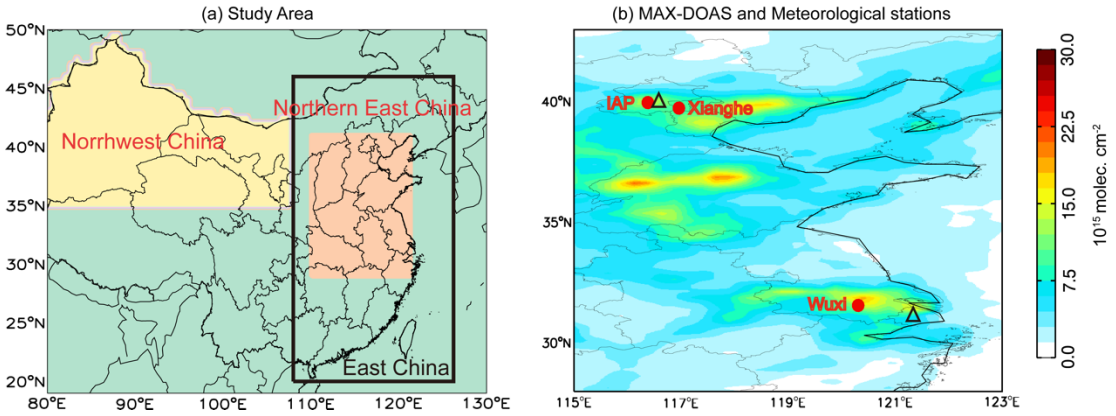

1025 Figure 1. (a) Three study areas: Northern East China, Northwest China, and East China.
1026 (b) MAX-DOAS measurement sites (red dots) and corresponding meteorological
1027 stations (black triangle) overlaid on POMINO v1.1 NO_2 VCDs in August 2012.

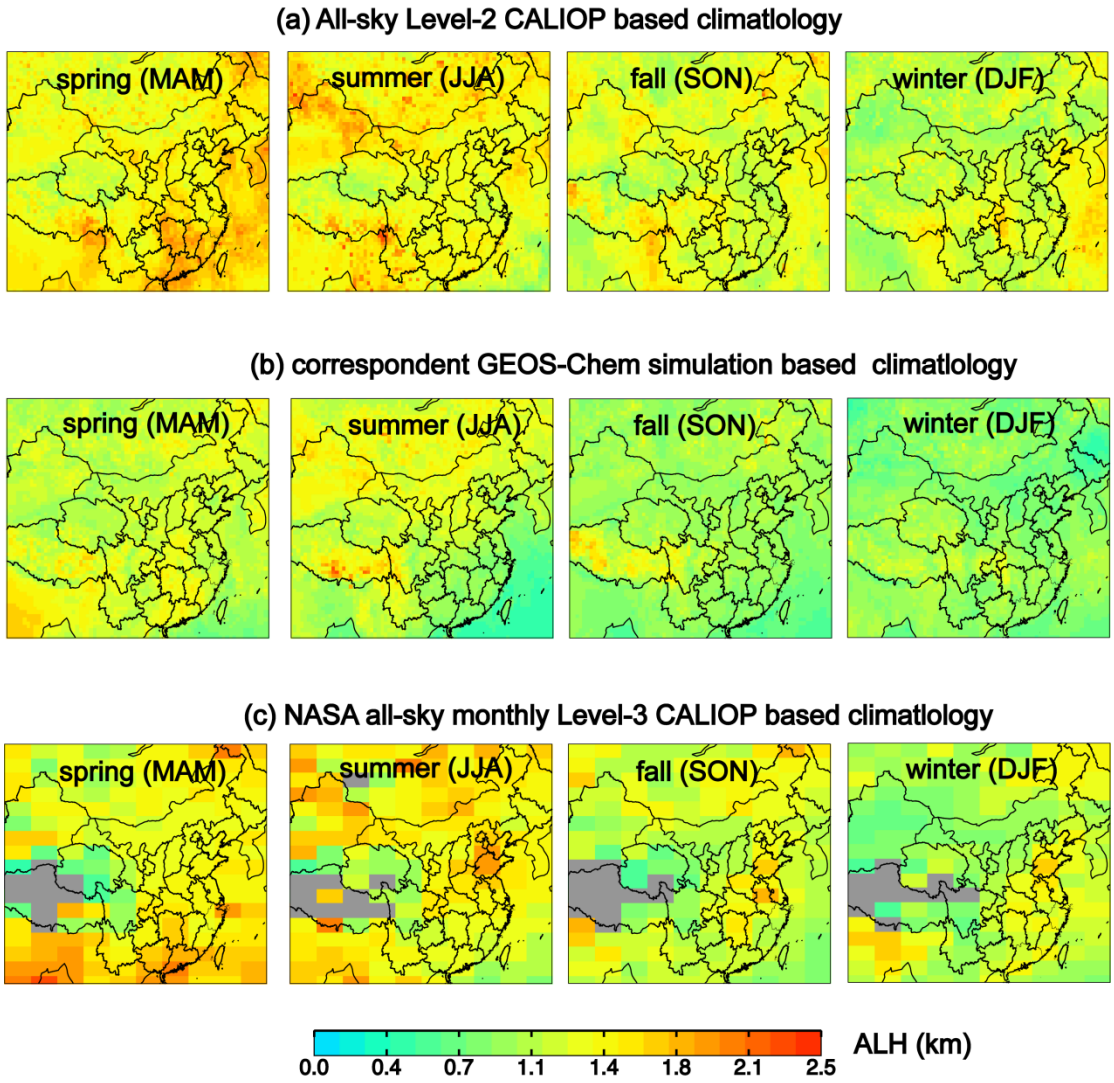

1028 Figure 2. Seasonal spatial patterns of ALH climatology at 532 nm on a 0.667° long. x
1029 0.50 ° lat. grid based on (a) our complied all-sky Level-2 CALIOP data, (b)
1030 corresponding GEOS-Chem simulations, and (c) NASA all-sky monthly Level-3
1031 CALIOP dataset.

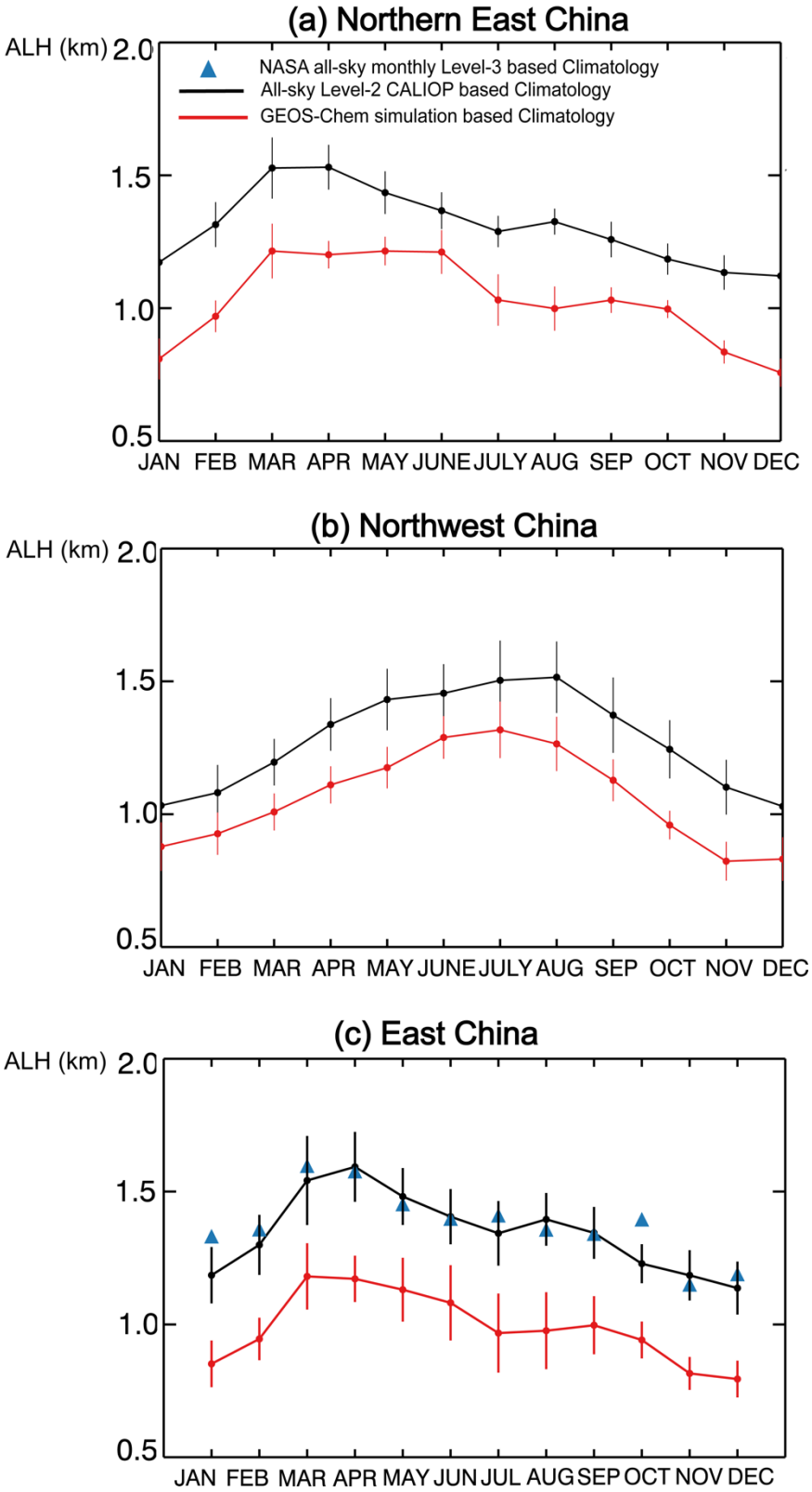

1032 Figure 3. Regional mean ALH monthly climatology over (a) Northern East China, (b)
1033 Northwest China, and (c) East China. The error bars stand for 1 standard deviation for
1034 spatial variability.

1035

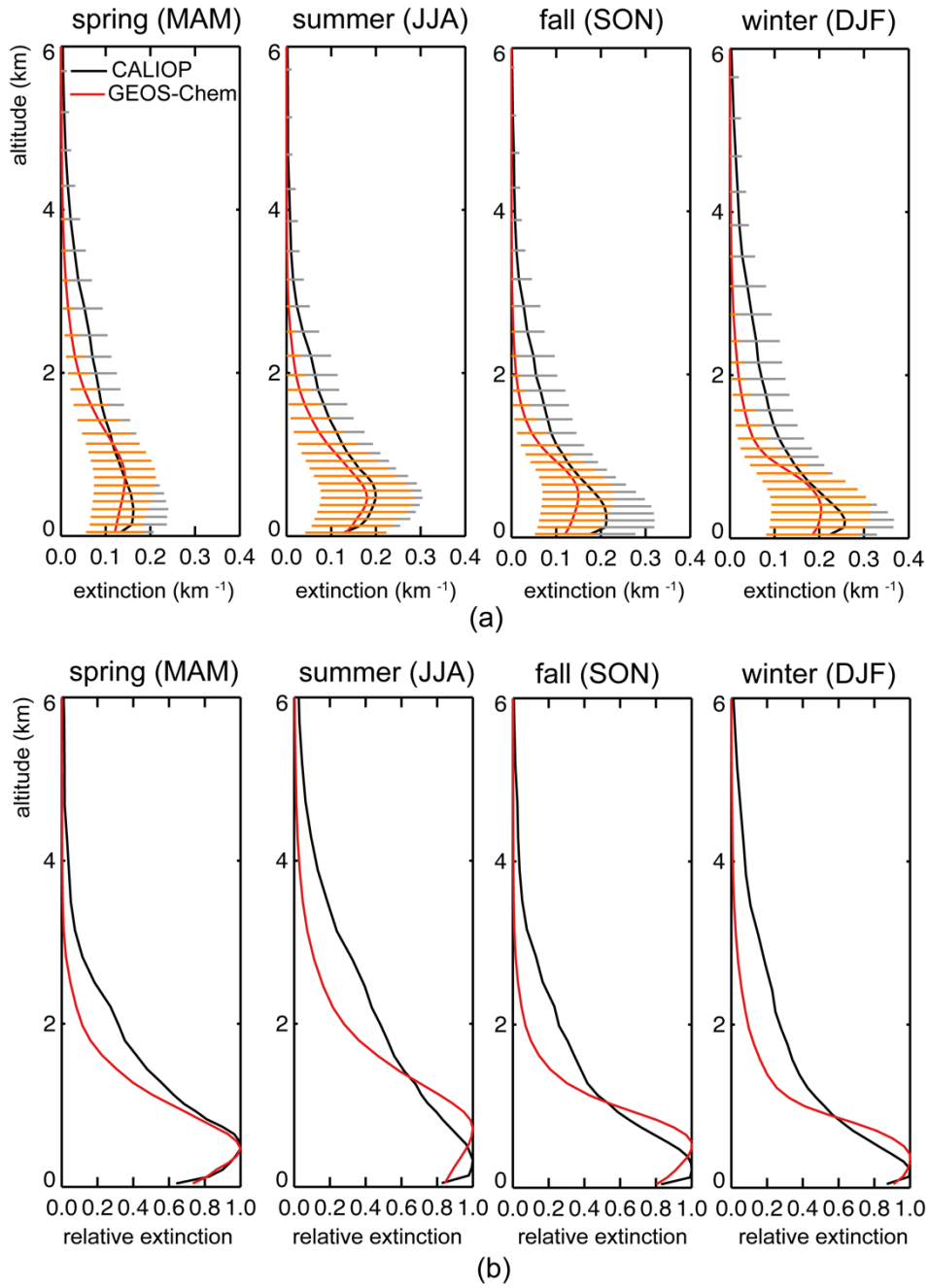

Figure 4. Seasonal climatological aerosol extinction profiles (first row) and corresponding relative extinction profiles (normalized to maximum extinction values, second raw) in spring (MAM), summer (JJA), fall (SON) and winter (DJF) over Northern East China. Model results (in red) are prior to MODIS/Aqua based AOD adjustment. Error bars in (a) represent 1 standard deviation across all grid cells in each season.

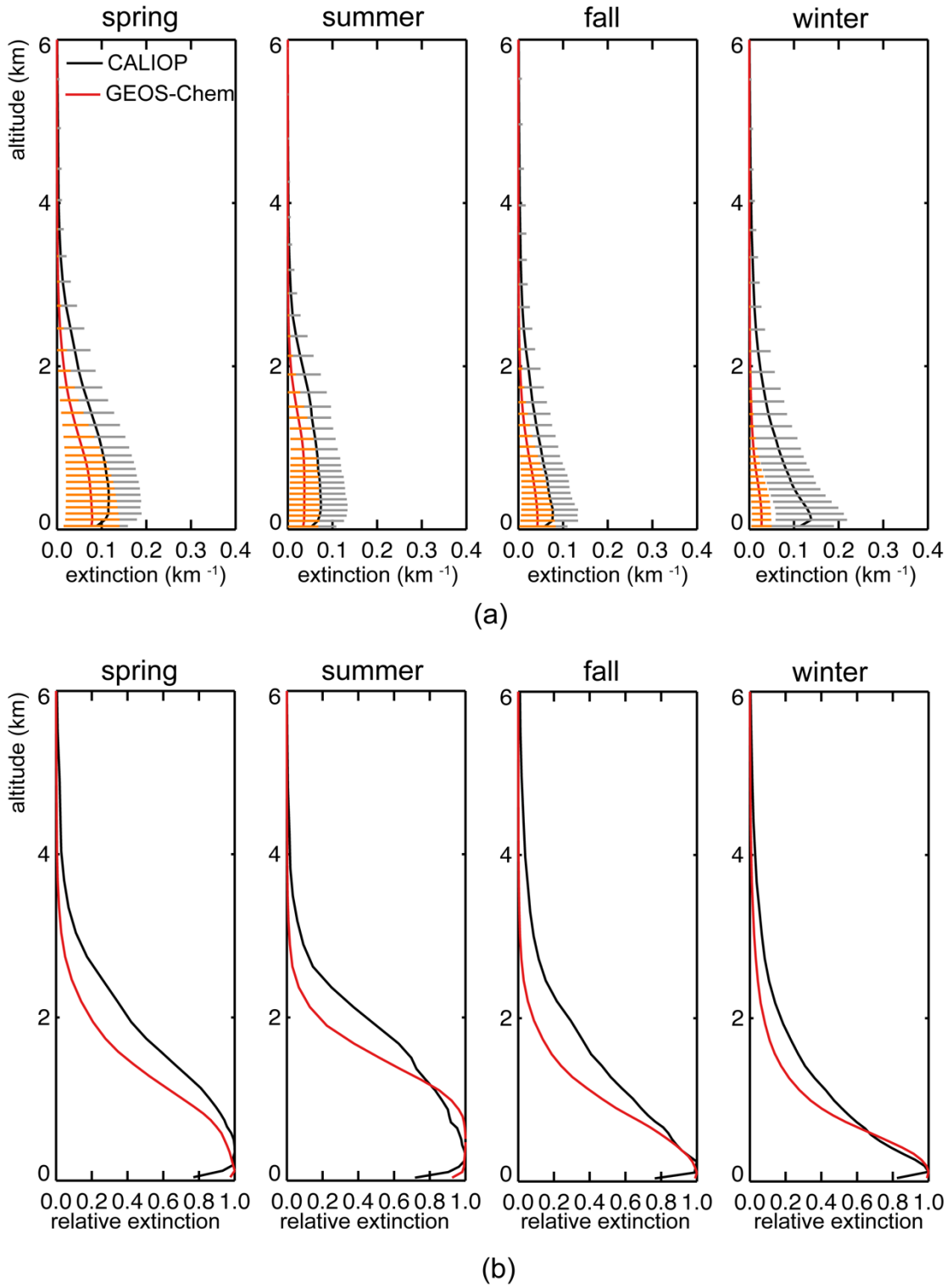

1042 Figure 5. Similar to Fig. 5 but for Northwest China.

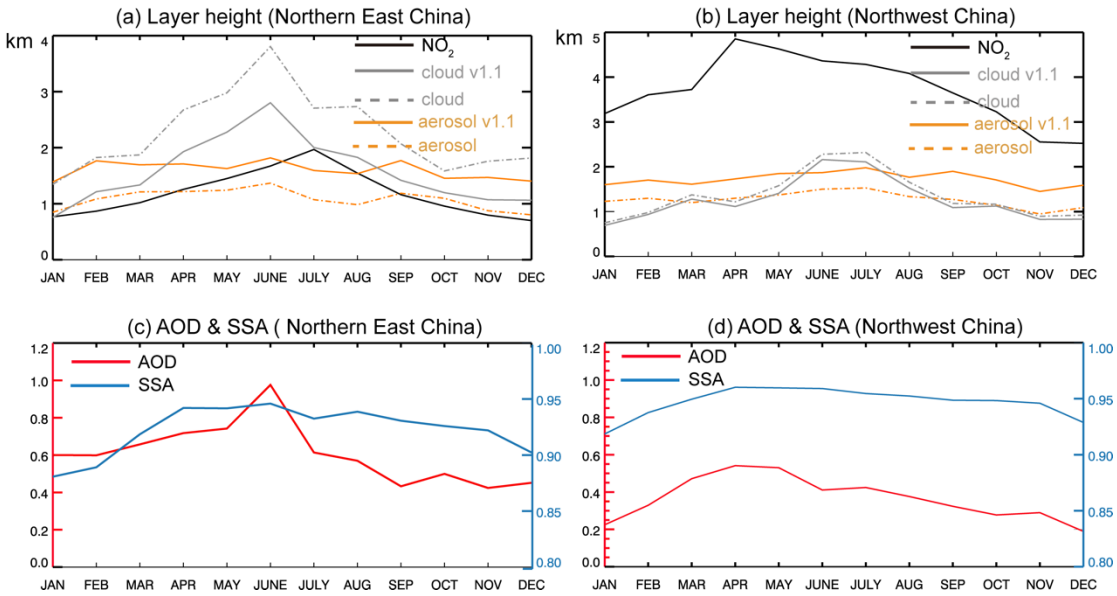

1043 Figure 6. Monthly variations of ALH, CTH and NLH over (a) Northern East China and
1044 (b) Northwest China in 2012. Data are averaged across all pixels in each month and
1045 region. The grey and orange solid lines denote POMINO v1.1 results, while the
1046 corresponding dashed lines denote POMINO. (c–d) Corresponding monthly AOD and
1047 SSA.

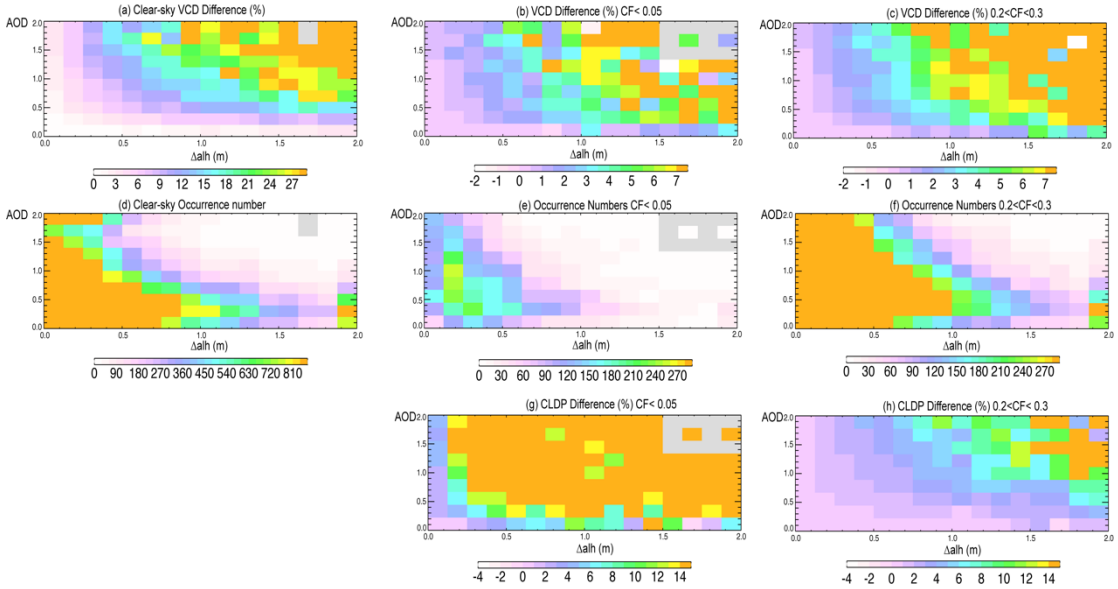

Figure 7. Percentage changes in VCD from POMINO to POMINO v1.1 ([POMINO v1.1 – POMINO] / POMINO) for each bin of ΔALH (bin size = 0.2 km) and AOD (bin size = 0.1) across pixels in 2012 over Northern East China, for (a) cloud-free sky (CF = 0 in POMINO), (b) little-cloudy sky, and (c) modestly cloudy sky. (d-f) The number of occurrences corresponding to (a-c). (g, h) Similar to (b, c) but for the percentage changes in cloud top pressure (CP).

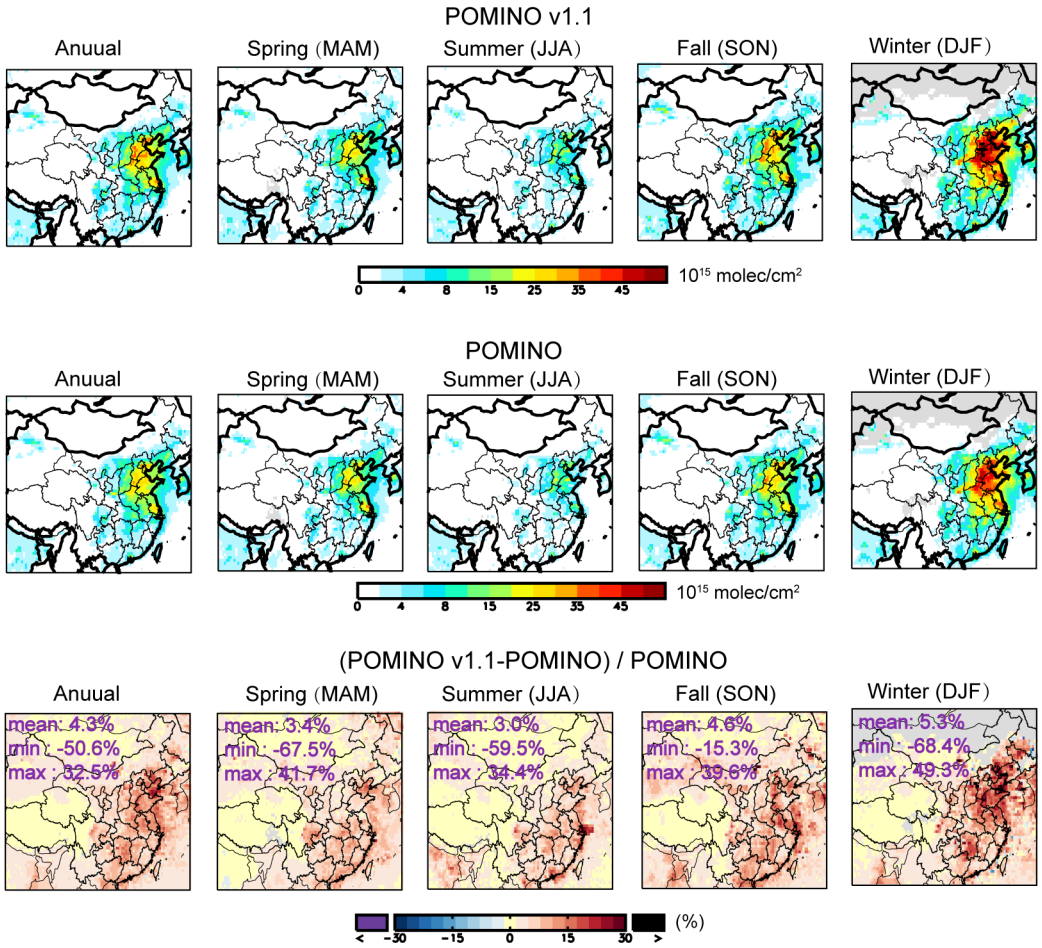

1054 Figure 8. Seasonal spatial distribution of tropospheric NO_2 VCD in 2012 for (a)
1055 POMINO v1.1, (b) POMINO, and (c) their relative difference.

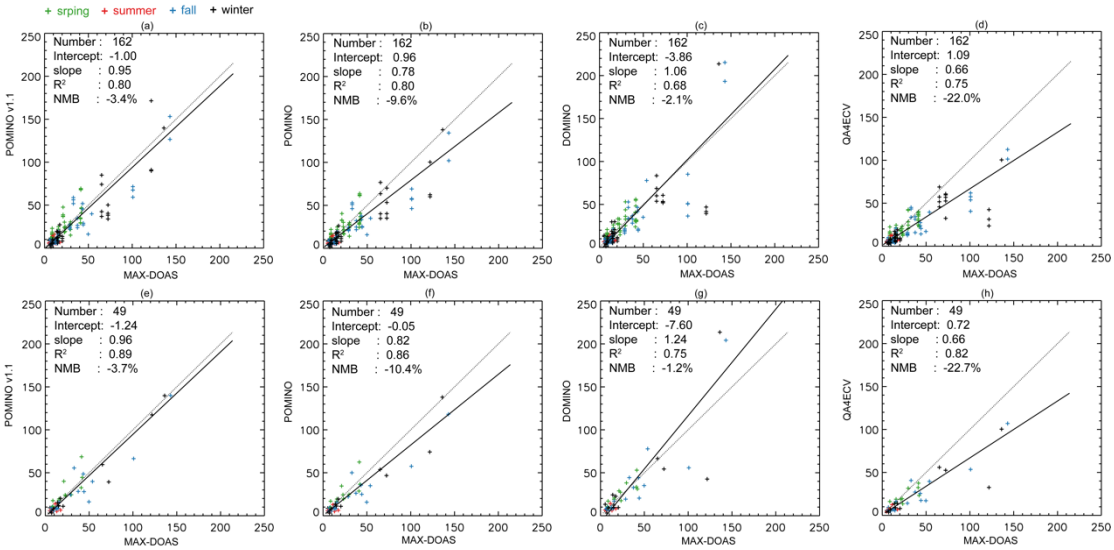

1056 Figure 9. (a–d) Scatterplot for NO_2 VCDs (10^{15} molec. cm^{-2}) between MAX-DOAS
1057 and each of the three OMI products. Each "+" corresponds to an OMI pixel, as several
1058 pixels may be available in a day. (e–h) Similar to (a–d) but after averaging over all OMI
1059 pixels in the same day, such that each "+" represents a day. Also shown are the statistic
1060 results from the RMA regression. The black solid line indicates the regression curve
1061 and the grey dotted line depict the 1:1 relationship.

1062

1063